NASA CR 120913
Report MDC Q0449
April 1972

# Testing Superalloys at 2000 (1367) and 2200°F (1478 K) in a Mach 4.6 Airstream

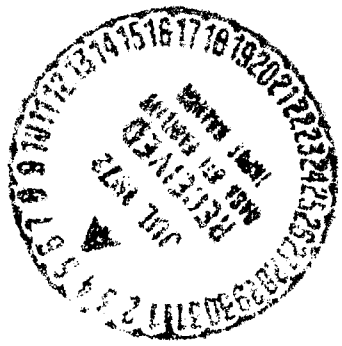

Donald W. Land
Ronald R. Williams
Walter A. Rinehart

Prepared for
National Aeronautics and Space Administration
NASA Lewis Research Center
Contract NAS3-14666-H
Dr. H.B. Probst, Project Manager



MCDONNELL DOUGLAS RESEARCH LABORATORIES

MCDONNELL DOUGLAS CORPORATION

NASA CR 120913
Report MDC Q0449
April 1972
Copy No. 20

# Final Report

# Testing Superalloys at 2000 (1367) and 2200°F (1478 K) in a Mach 4.6 Airstream

by

Donald W. Land, Ronald R. Williams and Walter A. Rinehart

Flight Sciences Department
McDonnell Douglas Research Laboratories
McDonnell Douglas Corporation
St. Louis, Missouri 63166

**Details of illustrations in this document may be better studied on microfiche**

Prepared for
National Aeronautics and Space Administration
April 1972
Contract NAS3-14666-H

NASA Lewis Research Center
Cleveland, Ohio
Dr. H. B. Probst, Project Manager
Oxidation and Refractory Compounds Section

# Foreword

The work described herein was performed by the McDonnell Douglas Research Laboratories under NASA Contract NAS3-14666-H. The NASA Project Manager was Dr. H.B. Probst, Head, Oxidation and Refractory Compounds Section, NASA Lewis Research Center.

# Contents



*This document consists of a title page, pages iii, v, vii and pages 1 through 41.*

# Abstract

Seven superalloy models were tested in the McDonnell Douglas Research Laboratories (MDRL) Plasma Arc Tunnel (PAT) facility. The test models were 3 in. (7.62cm) square flat surfaces (nominally 0.01 to 0.02 in. (0.0254 to 0.0508 cm) thick) held in a water-cooled wedge holder at a 60 deg (1.05 rad) angle of attack. The models were cycled 25 times (two were cycled 50 times) for 10 min each cycle in a Mach 4.6 test stream with the model leading edge temperature maintained at 2200°F (1478 K) (one at 2000°F (1367 K)). Backface temperatures were measured with four platinum-platinum 10% rhodium thermocouples and the front surface temperatures with an optical pyrometer. Four different nickel base alloy materials and one cobalt base material were evaluated.

# 1 Summary

This report describes the test program conducted in the McDonnell Douglas Research Laboratories (MDRL) where proposed space shuttle superalloy materials supplied by NASA Lewis Research Center were subjected to a high temperature plasma environment. The primary objective of this program was to obtain performance data during superalloy material tests at conditions existing on the orbiter lower surface during a low cross range entry.

A total of five different materials and seven different models were evaluated in the MDRL Plasma Arc Tunnel (PAT) facility. Pre-test oxidation was not performed on any of the models. Five models were cycled 25 times for 10 min each test cycle and two models were cycled 50 times each. The models were held with minimum contact in a (1.05 rad) angle of attack relative to the test stream centerline. The model leading edge temperature was maintained at 2200°F (1478 K) for all but one model which was controlled to 2000°F (1367 K) during all its test cycles.

The models were nominally 3.0 in. x 3.0 in. (7.62 cm x 7.62 cm) square flat plates 0.01 to 0.02 in. (0.0254 to 0.0508 cm) thick. They were retained by small pins and insulated from the water-cooled holder by Fiberfrax. Each model was instrumented on the backside with four platinum-platinum 10% rhodium thermocouples whose outputs were continuously measured during each test cycle. In addition, optical pyrometer measurements of the model front surface temperature were made at 13 surface locations on many test cycles.

The test environment was generated by the ohmic heating of dry air in a Hüls type hollow electrode arc heater with the high temperature air exhausting through an 8 in. (20.3 cm) diam exit Mach 4.6 conical nozzle into a 6 ft (1.83 m ) diam evacuated test chamber. Nominal arc heater parameters for the two test conditions of 2000 (1367 K) and 2200°F (1478 K) at the superalloy leading edge regions were power inputs of 174 kW and 196 kW, arc heater chamber pressures of 525 $\pm$ 10 Torr (7.0 x $10^4$ $\pm$ 133 $N/m^2$) and bulk enthalpies of 2450 (5.7 x $10^6$ J/kg) and 2800 Btu/lb (6.5 x $10^6$ J/kg) respectively. The bulk enthalpy was obtained by performing an energy balance on the arc heater. The cold wall heat flux at the model surface position (1 in.(2.54 cm) downstream of the wedge holder leading edge) corresponding to the equilibrium temperature measurement points of 2000 (1367 K) and 2200°F (1478 K) was 24.5 (2.78 x $10^5$) and 34.8 $Btu/ft^2$ sec (3.95 x $10^5$ $W/m^2$) respectively. The surface pressure at this same location for the two conditions was maintained constant at 9.7 Torr (1.3 x $10^3$ $N/m^2$).

Reported data include pretest and post-test weight and thickness measurements from which ablation rates may be derived and material temperatures to which the material properties can be referenced. The temperatures reported are from the optical pyrometer measurements and the continuous recordings of the four thermocouple outputs during each test cycle. A test cycle included the 10 min of heating plus the time required for the model to cool by radiation (typically 2.5 min) to a temperature of 400°F (478 K).

The greatest weight loss was experienced by the Haynes-188 material (a cobalt base alloy) even though it was tested at a less severe condition (2000°F) (1367 K) and two other materials were tested twice as long (50 cycles vs 25 cycles). However, total model test times were too short to provide definitive patterns in material performance based on weight loss measurements only.

Material degradation as determined by thickness change (gross measurement including scale) was not evident in these tests.

Optical pyrometer measurements were affected by the radiance from the arc chamber reflected off the model surface. As a result, it was not possible to determine model emittances by comparison of surface temperature pyrometer measurements and backface thermocouple measurements.

# 2 Introduction

The Flight Sciences Department of the McDonnell Douglas Research Laboratories (MDRL) performed a series of high temperature tests on superalloys in a Mach 4.6 moving airstream for NASA Lewis Research Center under contract NAS3-14666-H. These tests were conducted to provide the Oxidation and Refractory Compounds Section at NASA Lewis with thermal performance and mass change information on various superalloys being investigated for potential use on the space shuttle. Previous evaluation tests in an arc heater facility on similar superalloy materials were conducted at NASA Ames.[1]

All material tests described herein were conducted in the 2 MW Plasma Arc Tunnel (PAT) facility of MDRL, located in St. Louis, Missouri. The test period extended from November 1970 through May 1971. The models tested have been arbitrarily assigned numbers 1 through 7, which indicates the receiving order from NASA Lewis. Model testing was conducted in the same order. Further identification of the models is contained in Section 5 of this report.

Five different alloys and seven total samples were tested under this contract. The arc heater operating condition was stabilized prior to inserting each sample in the high temperature flow. As each 10 min test cycle was completed, the sample was indexed out of the test stream and allowed to cool to at least $400^{0}$F (478 K) before it was reinserted. The arc heater operation was continuous except for shutdown for periodic examinations of the sample surface and insulation packing.

The steady-state temperature at the leading edge was achieved in approximately 100 sec after the sample was inserted into the test stream. During each cycle the backface temperatures were recorded continuously at a scanning rate of six times each per minute. Front surface temperatures were measured at least every fifth cycle at 13 locations on the sample surface using an optical pyrometer.

This report presents a description of the test facility, model configurations, instrumentation, operational procedure, and results for the test program.

# 3 Apparatus



## 3.1 PAT facility

The McDonnell Douglas PAT facility (Fig. 1) consists of a Hüls type arc heater, model actuator, 6 ft (1.83 m) diam water-cooled vacuum tank, six-stage steam ejector system, power, water, and air supplies, and associated instrumentation.

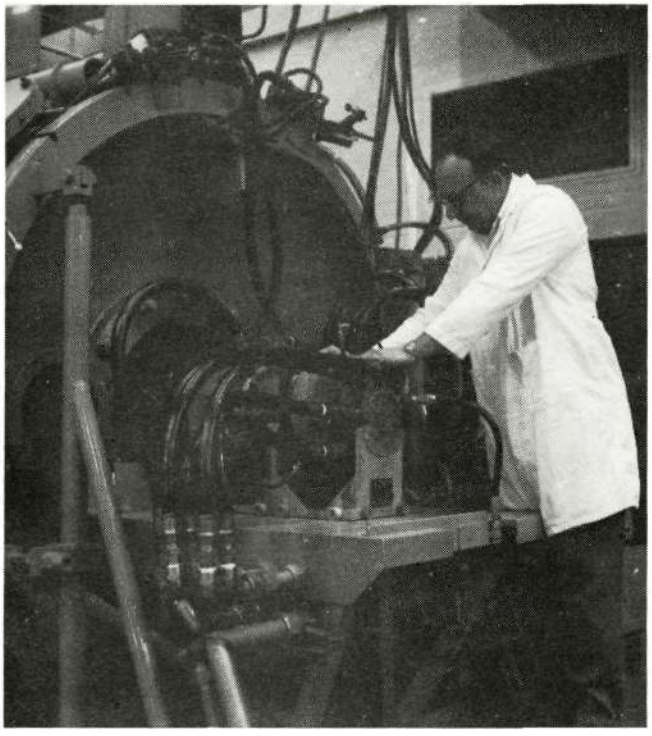

Fig. 1 Plasma arc tunnel (PAT) facility

### 3.1.1 Arc heater

The arc heater currently used in the PAT facility is a Hüls type, dc powered arc heater with tandem, water-cooled, cylindrical hollow electrodes. Table I shows the range of arc heater operating parameters. The electrode materials used primarily for this contract were OFHC copper with 20% Cu - 80% Ag alloy inserts. Contamination resulting from electrode erosion is small (less than 0.1% by weight ratio to the air flow rate) even at high operating currents (2000 A). In this type of heater, the largest percentage of electrode erosion occurs during arc heater start-up and stabilization; therefore, the ability to operate the heater continuously for long periods at constant conditions resulted in sizeable reductions in total electrode erosion. For this program the total electrode erosion was only 0.0077% by weight.

Several nozzles are available for use with the PAT facility. The exit diameters range from 1.25 to 8.00 in. (3.17 to 20.32 cm). They are all conical convergent-divergent nozzles and provide flow up to Mach 5.9. The nozzle used for this program had an 8.00 in. (20.32 cm) diam exit with a 1.00 in. (2.54 cm) diam throat, and provided Mach 4.6 flow.

Figure 2 shows the PAT facility test stream capabilities for both splash and wedge model configurations. Figure 2b illustrates the heat flux-surface pressure capability on a wedge model using the 8 in. (20.32 cm) exit diam nozzle and air as the test gas. The envelope represents the model surface conditions 1.0 in. (2.54 cm) from the wedge leading edge with the wedge angle varied from 5 to 60 deg (0.09 - 1.05 rad). Some measured data are shown for nominal test stream Mach numbers of 4.6

**Table I PAT facility arc heater operating range**

| Parameter | Range of operation | Operating parameters at | | |
|---|---|---|---|---|
| | | Maximum bulk enthalpy | Maximum chamber pressure | Maximum power input |
| Bulk enthalpy Btu/lb (J/kg) | 2000 - 29,000 ($4.65\times10^6$ - $6.75\times10^7$) | 29,000 ($6.75\times10^7$) | 2800 ($6.5\times10^6$) | 3400 ($7.5\times10^6$) |
| Chamber pressure atm ($N/m^2$) | 0.09 - 56.5 ($9.1\times10^3$ - $5.72\times10^6$) | 0.18 ($1.8\times10^4$) | 56.5 ($5.72\times10^6$) | 35.8 ($3.63\times10^6$) |
| Power input (MW) | 0.065 - 2.33 | 0.19 | 1.83 | 2.33 |
| Air flow rate lb/sec (kg/sec) | 0.0023 - 0.289 (0.0010 - 0.131) | 0.003 (0.0014) | 0.238 (0.108) | 0.281 (0.128) |
| Arc current (A) | 183 - 2000 | 620 | 810 | 1040 |
| Arc voltage (V) | 106 - 2260 | 305 | 2240 | 2240 |
| Efficiency (%) | 12 - 71 | 49 | 41 | 45 |
| Nozzle throat diam in. (cm) | 0.250 - 1.000 (0.636 - 2.54) | 0.984 (2.50) | 0.250 (0.636) | 0.375 (0.954) |
| Exit Mach no. | 1.0 - 5.9 | 1.0 | 4.1 | 3.5 |

and 5.9, achieved by using different nozzle throat modules having diameters of 0.55 (1.397 cm) and 1.00 in. (2.54 cm). The two test conditions used on this contract are also shown.

### 3.1.2 Model actuator

The water-cooled model actuator system shown schematically in Fig. 3 can accomodate up to three test models per facility run. The model actuator arms are spaced 90 deg (1.57 rad) apart and can be indexed into the test stream either clockwise or counterclockwise. The axial position of the entire system can be varied 12 in. (30.5 cm) during a run. All model actuator controls can be remotely operated from the PAT control room or can be activated at the vacuum tank test area. Each model arm position is indicated electronically on the data recording system to within 0.05 sec of its locked, centerline position.

All model instrumentation can be protected by directing it through the center of the water-cooled support arms. Provisions can be made for testing at various angles of attack.

### 3.1.3 Subsystems

**Vacuum Tank** - The vacuum tank is 6 ft (1.83 m) in diam and 27 ft (8.2 m) long. A 3 ft (0.9 m) diam door on either side of the test section provides easy access for model installation. Each door has two 12 in. (30.5 cm) diam windows for model observation during test. An overhead port is also available for model observation with either a camera or optical pyrometer. The entire tank is double-walled and water-cooled. Two heat exhangers at the end of the tank cool the effluent before it goes to the steam ejectors.

**Steam ejectors** - The six-stage noncondensing steam ejector system was designed and built by the Croll-Reynolds Company of Westerfield, New Jersey. The first three stages are designed to operate at 185 psig ($1.28 \times 10^6$ $N/m^2$) with 50°F (283 K) superheated steam. Stages 4 through 6 are designed to operate at 185 psig ($1.28 \times 10^6$ $N/m^2$) saturated steam. The total steam consumption for this system is approximately 62,000 lb/hr (7.8 kg/sec). The system performance characteristics for air are shown in Fig. 4. The minimum blank off pressure is 0.01 Torr (1.33 $N/m^2$).

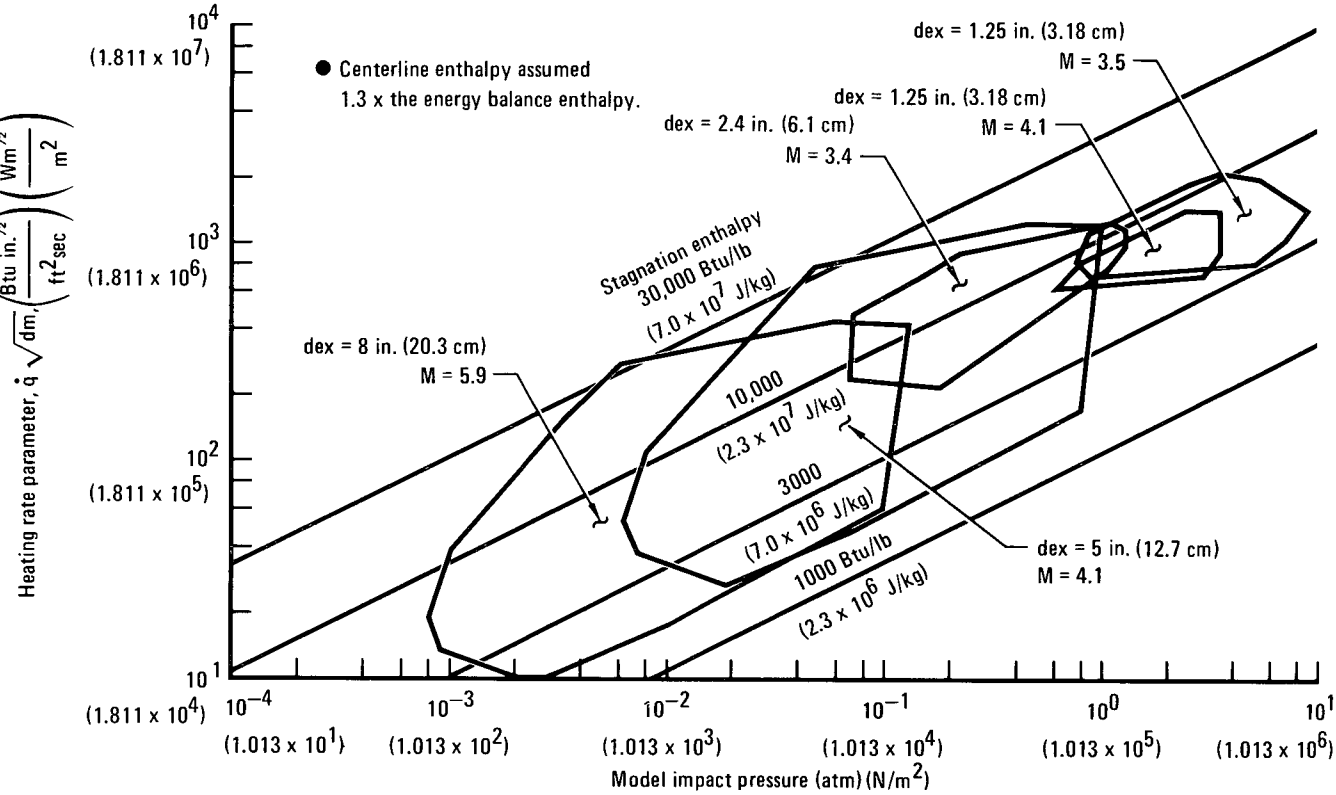


(a) Flat face model

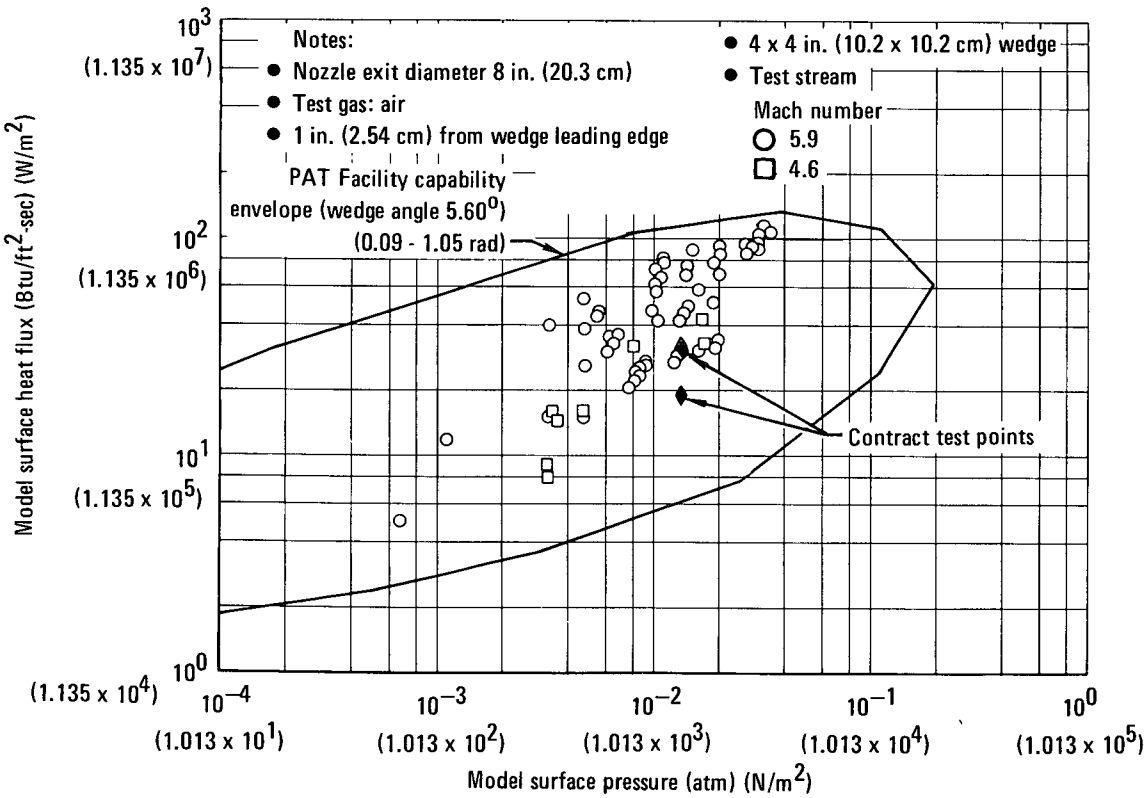


(b) Wedge model

**Fig. 2 PAT facility testing capability**

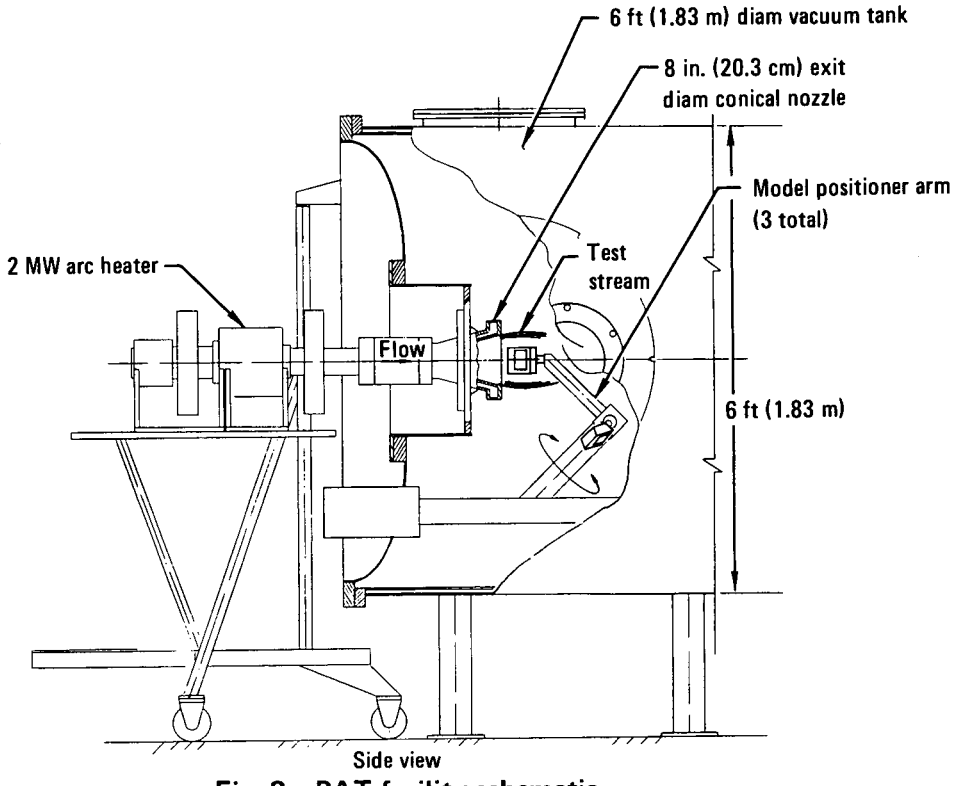


Fig. 3a PAT facility schematic

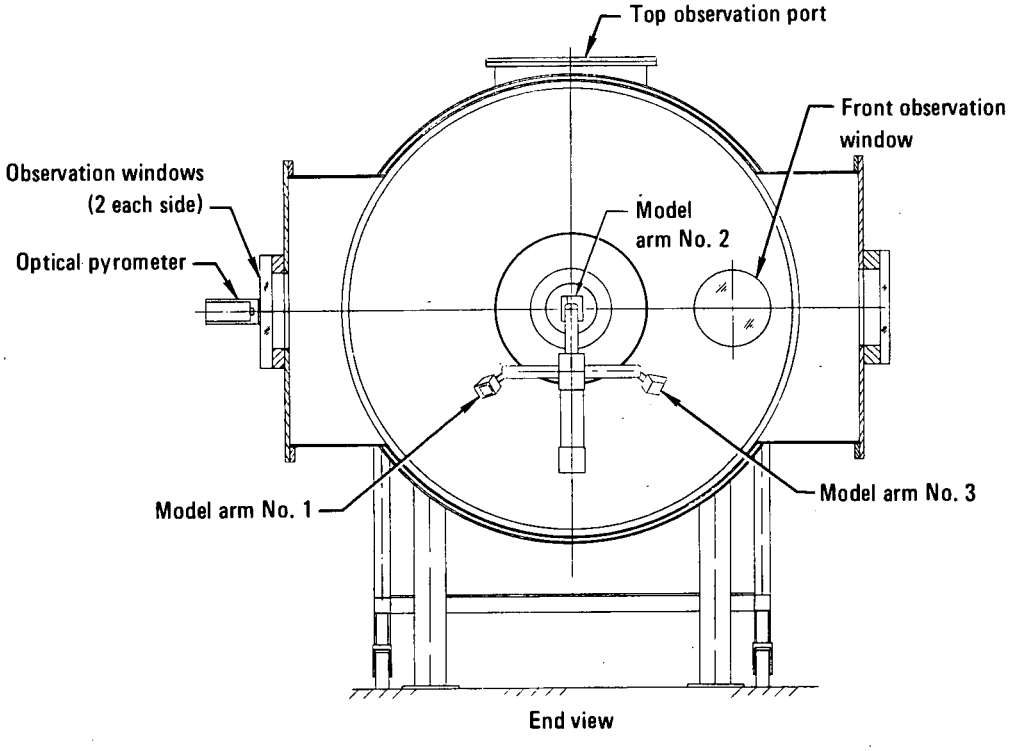


Fig. 3b PAT facility schematic

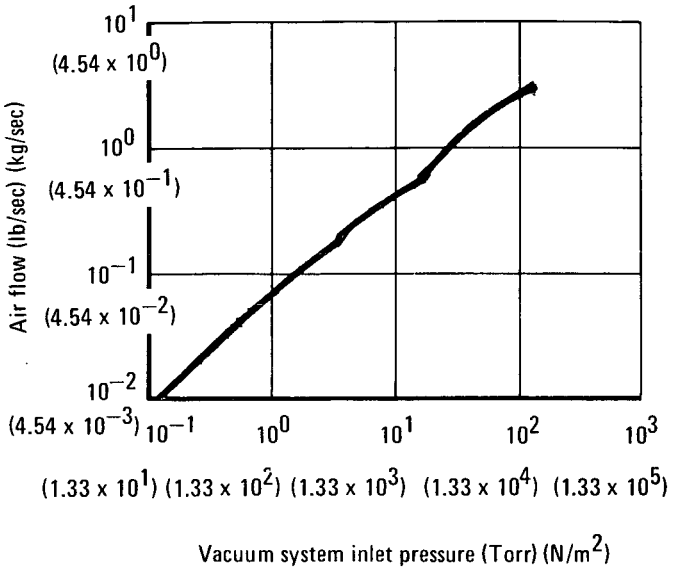


**Fig. 4 Steam ejector pumping characteristics for air**

**Power supply** - Two A.O. Smith power supplies, each having a 600 kW continuous nominal power rating and a maximum continuous rating of 750 kW when operating at approximately 80% of the open circuit voltage, are used for operating the arc heater. In addition, a maximum output of 1.67 mW can be obtained from each unit for 30 sec. Each power supply is a three-phase full wave rectifier and has a saturable reactor current control to provide the drooping output characteristics shown in Fig. 5. The open circuit voltages are 250, 500 1000, and 2000 V. Two of the four voltage and current output ranges available are shown in Fig. 5. The power supplies for this program were in parallel resulting in an open circuit voltage of 2000 V. The power supplies can also be operated in series which doubles the open circuit voltage.

**Air supply** - The air supply system provides clean, dry, filtered air to the arc heater up to pressures of

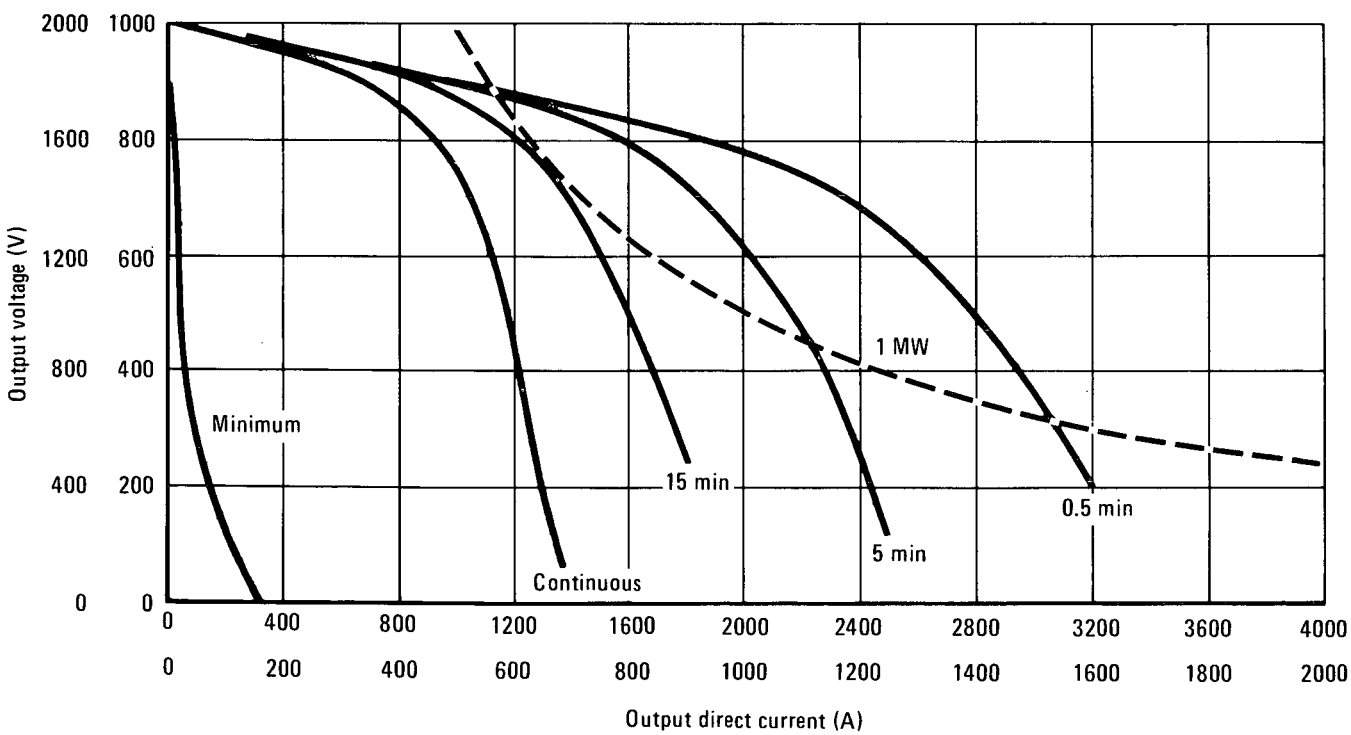


**Fig. 5 Power supply performance characteristics (one unit)**

3600 psig (2.48 x $10^7$ N/$m^2$). Up to 4.0 lb/sec (1.8 kg/sec) air flow can be obtained from the system, but normal flow rates for the PAT facility are less than 0.25 lb/sec (0.11 kg/sec). Continuous flow regulation is provided, and flow rates are measured using critical Venturi (choked nozzle) flowmeters which are calibrated against a flowmeter calibrated by the U.S. Bureau of Standards. For these tests, two air flowmeters were used: a 0.082 in. (0.208 cm) diam throat flowmeter for the primary flow, and a 0.070 in. (0.178 cm) diam throat flowmeter for the secondary flow. Secondary flow enters the arc heater downstream of the arc and is used to provide lower bulk enthalpy test streams than normal arc heater operation allows.

**Water supply** - Water is supplied to the arc heater from a multistage Gould centrifugal pump. Up to 1200 gpm (7.6 x $10^{-2}$ $m^3$/sec) is available at a pressure of 550 psig (3.8 x $10^6$ N/$m^2$). Only a portion of this supply is required for the arc heater. Cooling water for the model actuator and arc heater spin coils comes from the same source but is regulated to a lower pressure. Heat exchanger and vacuum tank cooling water come from a separate nonregulated source.

## 3.2 Model description

### 3.2.1 Models

All test material was furnished by NASA Lewis, but the models were shaped at MDRL. The seven models tested had different chemical compositions; six were nickel base alloys and one was cobalt base. The model configuration was basically a flat plate nominally 3 in. x 3 in. (7.6 cm x 7.6 cm) with a 0.09 in. (0.23 cm) 90 deg (1.57 rad) radius along each edge. At the midpoint of each edge, a 0.25 in. (0.64 cm) square tab extended from the radius for attaching the model in the holder. Each tab had a small hole to accommodate retaining pins extending from the model holder. This final test model configuration resulted from several in-house attempts to find a stable design which allowed a minimum of surface distortion when cycled to 2200°F (1478 K).

The material used for the model configuration in-house preliminary tests was TD-NiCr. Three of the trial configurations are shown in Fig. 6 with the center model configuration being the one finally selected for this program.

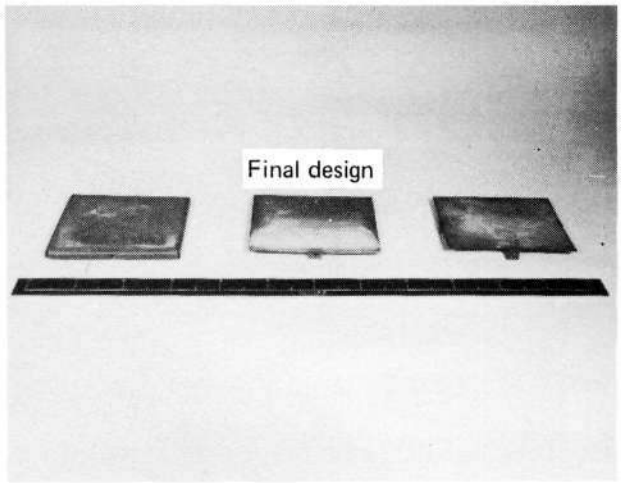


**Fig. 6 Trial model configurations**

Special forming jigs were designed for use in shaping the model while protecting the test surface from damage.

### 3.2.2 Wedge holder

The wedge holder (Fig. 7) was a water-cooled copper body 4 in. x 4 in. (10.2 x 10.2 cm) with a sharp leading edge. A cavity 3.06 in. (7.77 cm) square was centrally located and was 1 in. (2.54 cm) deep to accommodate model instrumentation and backface insulation. A pin on the wedge at the midpoint of the model leading edge and three adjustable retaining pins at the midpoint of the sides and trailing edge provided support and positioning of the test model. The location of these pins allowed the model to expand and contract freely. The small pin to model contact area minimized thermal losses from the model. Four adjusting screws, perpendicular to the model surface and passing through the wedge

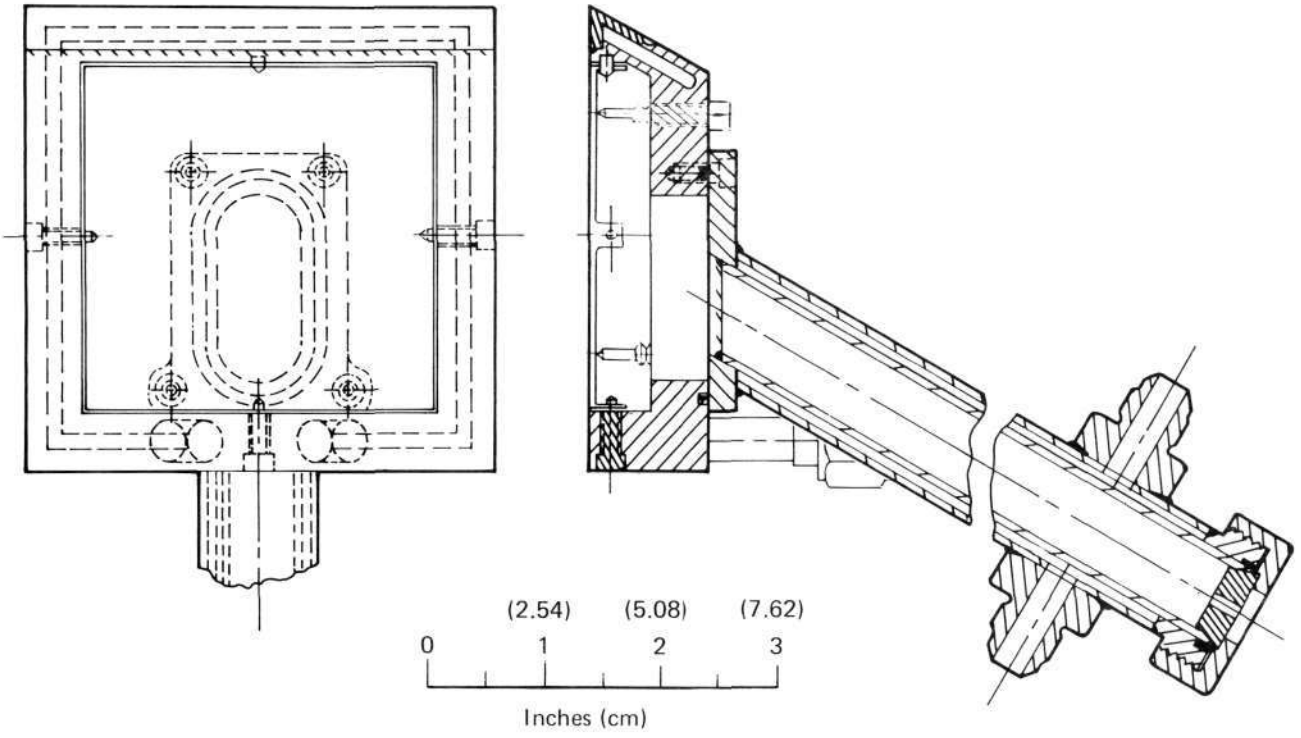


**Fig. 7 Superalloy model holder**

holder backface and insulation cavity provided additional support for each model quadrant. These screws had small pointed tips to minimize heat losses.

The wedge model holder was mounted to the model actuator arm with a water-cooled sting. The sting was designed to hold the wedge and model test surface at a 60 deg (1.05 rad) angle of attack with the sample center on the axial centerline of the test stream. Figure 8 shows the wedge holder with a typical test model installed.

### 3.2.3 Calibration plates

A 3 in. x 3 in. (7.6 x 7.6 cm) flat surface copper plate simulating the superalloy test models was used to measure the cold wall heat flux distribution. Located on the plate were five oxygen-free high conductivity copper sensors as shown in Fig. 9.

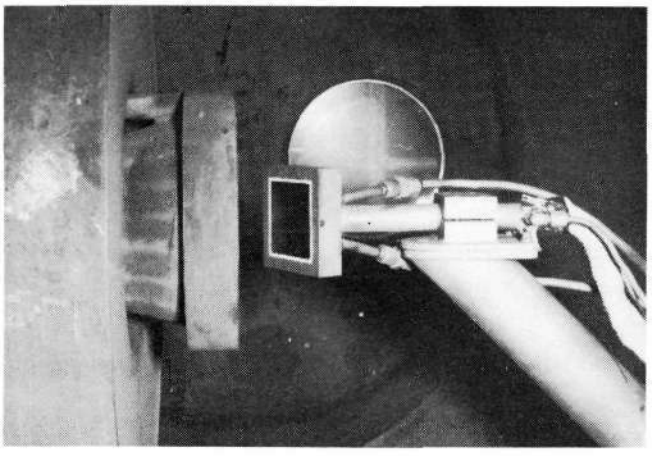

**Fig. 8 Typical model in test position**

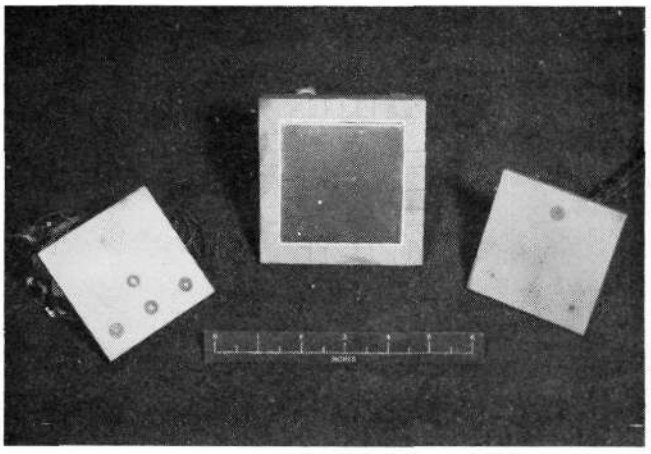

**Fig. 9 Calibration plates and typical model in holder**

These calorimeter slugs, 0.125 in. (0.318 cm) in diameter and length, provided transient measurements of the cold wall heat flux. The average slug temperature was sensed by a 30 gauge chromel-alumel thermocouple peened into holes in the slug base. The heat flux at each slug position was calculated using the following relationship:

$$\dot{q}_{cw} = \frac{mC_p}{A}\frac{\Delta T}{\Delta t},$$

where

$\dot{q}_{cw}$ = heat flux (cold wall) - Btu/ft$^2$ sec (W/m$^2$)
m = mass of the calorimeter slug - lb (kg)
A = calorimeter sensing area - ft$^2$ (m$^2$)
$C_p$ = temperature averaged heat capacity of copper - Btu/lb$^o$F (J/kg K)
$\frac{\Delta T}{\Delta t}$ = slug temperature rise rate - $^o$F/sec (K/sec)

Thermal errors were minimized by mounting each sensor in a centering transite support and then sealing the surface with a fine mixture of Sauereisen No. 8 cement.

Model surface pressures were measured at the five 0.030 in. (0.076 cm) diam static ports shown in Fig. 9. The ports were connected to 0-1 psid (0 - 6.9 x 10$^3$ N/m$^2$) Statham No. UGP4-L transducers via 1/8 in. (0.318 cm) o.d. copper tubing. The response time of the system was approximately 2 sec. The absolute static surface pressure was the pressure measured with the 0-1 psid (0 - 6.9 x 10$^3$ N/m$^2$) transducer plus the test chamber ambient pressure.

The measured heat flux and surface pressure distributions are shown in Fig. 10. Also shown are the predicted distributions using McDonnell Douglas Automation Company computer program KAIS.

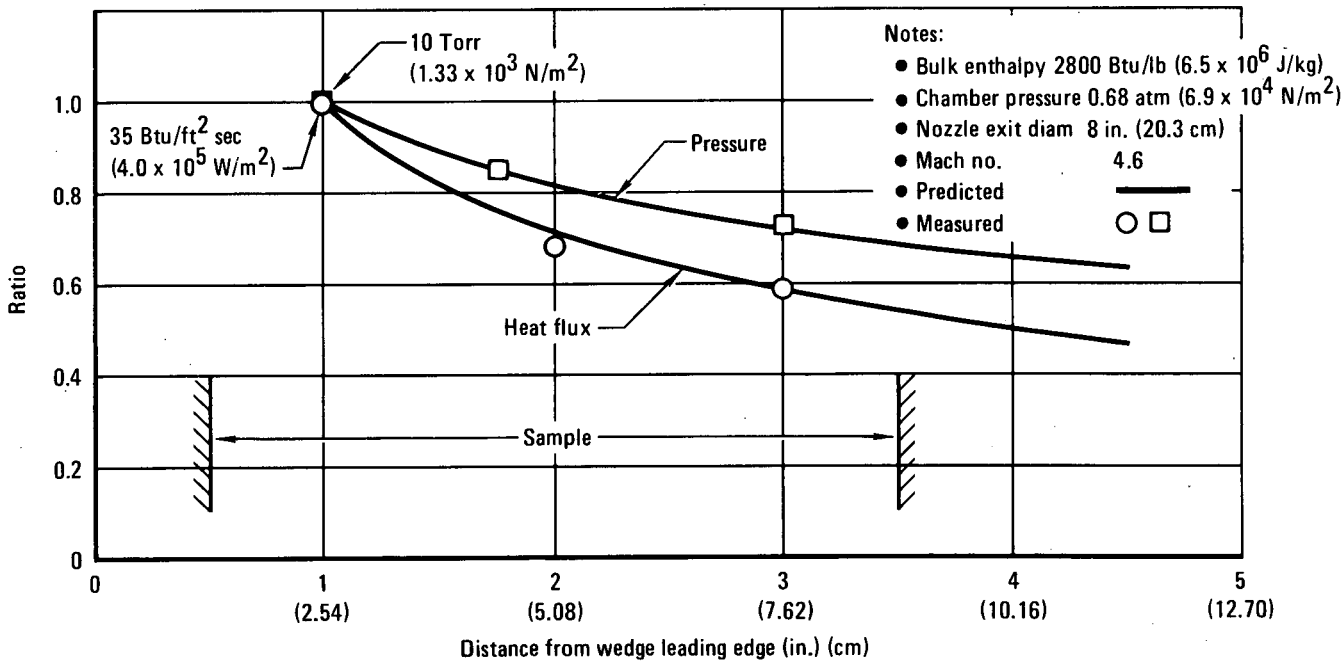


**Fig. 10 Heat flux and pressure distributions along 60 deg (1.05 rad) wedge surface centerline**

## 3.3 Instrumentation

The PAT facility was fully instrumented to provide permanent signal recordings as well as instantaneous visual readouts during a test. A maximum of 100 channels of data could be recorded on magnetic tape using the Central Data Acquisition System (CDAS). The maximum sampling rate per channel was equivalent to the system basic rate of 10,000 samples per second divided by the number of signal inputs.

### 3.3.1 Facility instrumentation

Recorded arc heater parameters included arc voltage, current, arc chamber pressure, primary and secondary flow pressures, cooling water flow rates, and cooling water temperature changes. A summary of the instruments used to record these and other parameters along with their accuracies are contained in Table II. The sensing elements used to measure the arc heater parameters have been calibrated by the McDonnell Aircraft Company (MCAIR) Calibration Laboratory or the MCAIR Bureau of Standards.

The energy balance bulk enthalpy is calculated from the above recorded arc heater parameters. The bulk enthalpy of the test gas is determined by subtracting the heat losses in the arc heater and nozzle from the total input power, and dividing the resulting net power by the gas mass flow rate.

**Table II Instrumentation**

| Parameter | Instrument | Recorder | Range | System accuracy |
|---|---|---|---|---|
| Arc heater | | | | |
| Arc pressure | CEC type 4-326-0031 | CDAS* | 0-50 psia ($0-3.4\times10^5$ N/m$^2$) | ±0.35% |
| Arc voltage | MDC voltage divider | CDAS | 0-2000V | ±0.35% |
| Arc current | GE model JDC-1 current transformer | CDAS | 0-1000A | ±0.75% |
| Primary air flow | MDC sonic flowmeter | CDAS | $10^{-3}$–$10^{-1}$ lb/sec ($4.5\times10^{-4}$–$4.5\times10^{-2}$ kg/sec) | ±1.0% |
| Secondary air flow | MDC sonic flowmeter | CDAS | $10^{-3}$–$10^{-1}$ lb/sec | ±1.0% |
| Arc heater ΔT | Delta T's | CDAS | 0-100°F (0-311K) | ±0.30% |
| Water flow rates | Turbine meters | CDAS | 0-70 gpm ($0-4.4\times10^{-3}$ m$^3$/sec | ±0.55% |
| Test model | | | | |
| Surface temperature | Infrared Industries model TD-9H pyrometer | CDAS | 1740 - 8300°F (1222 - 4867K) (3 scales) | ±1.0% F.S. (2740°F) (1777K) low scale |
| Backface temperature | Engelhard Industries standard grade, 30 gauge Pt/Pt 10% Rh thermocouple wire | CDAS | 0-3000°F (0-1922K) | ±1.9°F (1.06 K) |
| Surface pressure | Statham model no. UGP4-L | CDAS | 0-1 psid ($0-6.9\times10^3$ N/m$^2$) | ±0.00325 psi (22.4 N/m$^2$) |
| Weight | Voland 220 analytical balance | | 0-220 g | ±0.001 g |
| Thickness | Starrett micrometer | | 0.001-3.0 in. (0.00254-7.62 cm) | ±0.0005 in. (0.00127 cm) |

*Central Data Acquisition System

### 3.3.2 Model instrumentation

The backface temperature of the superalloy models was measured at four locations using standard grade Pt-Pt 10% Rh thermocouples. The thermocouple locations are shown in Fig. 11. Each thermocouple junction was formed by tack welding the two 30 gauge thermocouple wires to the model with the contacting ends parallel to the material grain direction and the last contact point being the required distance downstream of the sample leading edge. The thermocouple wires near the junctions were insulated with short hollow cylinders of alumina to prevent electrical shorts and reduce thermal energy losses. The remainder of the wires were insulated with Teflon spaghetti tubing.

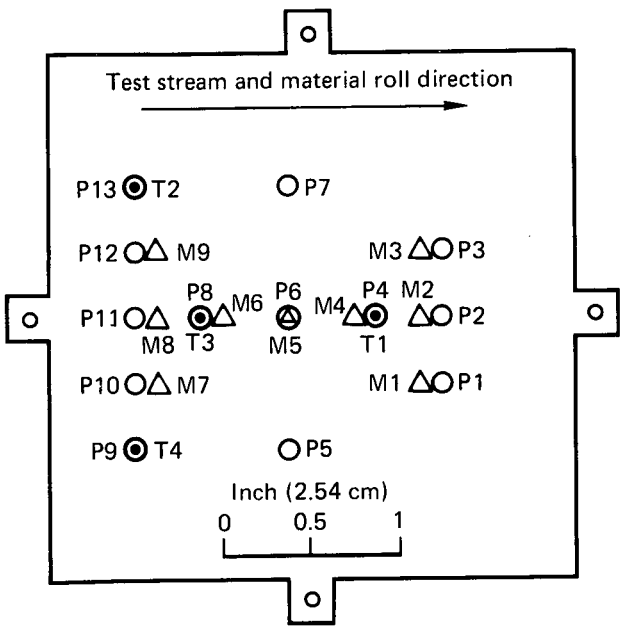


- ● Pt/Pt 10% Rh thermocouples (4)
- ○ Optical pyrometer readings (13)
- △ Thickness measurements before and after tests (9)

**Fig. 11 Model temperature and thickness measurement locations**

A typical thermocouple junction as described was calibrated in the MCAIR Bureau of Standards Lab and found to have a deviation of $\pm 3.6^{\circ}$F (2 K) in the range of 1800 to 2500°F (1256 to 1672 K) referenced to a premium grade Pt-Pt 10% Rh thermocouple that had been calibrated by the National Bureau of Standards. Each thermocouple was connected to an electronic 150°F (339 K) thermocouple reference junction compensator. The calibration of the reference junction was performed by MCAIR Calibration Laboratory and showed the reference temperature to be $150 \pm 0.5^{\circ}$F ($339 \pm 0.3$ K).

The CDAS recording system electrical noise was approximately ±5 counts which in the 2200°F (1478 K) temperature range represents a $\pm 1.8^{\circ}$F (1 K) deviation. An estimate of the maximum uncertainty of the indicated model backface temperature would be the summation of the individual errors, or $\pm 5.9^{\circ}$F (3.3 K). The most probable error, however, is equal to $\pm 1.9^{\circ}$F (1.1 K). This estimate of temperature error does not include effects of thermal gradients in the surface oxides and alloy materials, or the thermocouple errors associated with high temperature material diffusion at the junction.

Stable thermocouple outputs while the model was in the plasma test stream were the result of a grounding technique developed in the MDRL labs. This method of grounding eliminated induced signal noise, thus permitting the arc heater operator to make the necessary minute changes in operation and maintain the model backface temperature within $\pm 20^{\circ}$F (11 K) of the desired value. Continuous recordings of the thermocouple signals were made for each model during each cycle at a scan rate of six times per minute until midway through the cycle. The scan rate was then increased to 60 times per minute during the recording of optical pyrometer surface temperature distribution measurements.

An Infrared Industries Model TD-9H pyrometer was used to remotely measure the surface temperature distribution. Measurements were made at 13 locations shown in Fig. 11. A silicon photovoltaic detector is employed in this pyrometer to generate a signal voltage proportional to the radiation intensity of the target material. The signal voltage was recorded continuously on the CDAS. The pyrometer operates at a wavelength of 0.8 μm by using a spike filter. The spot size at the model surface

was determined from the following relationship:

$$\text{spot size} = \frac{\text{distance from object}}{330}$$

For the model-pyrometer configuration used in this test program the spot size was 0.12 in. (0.31 cm).

### 3.3.3 Central Data Acquisition System (CDAS)

A portable signal conditioning and digitizing station was located at the PAT facility and transmitted data in digital form to the central unit of the CDAS for recording on a tape transport. The system has the capability of recording and displaying 100 individual data input channels. The maximum sampling rate was 10 samples per channel per second although this speed was not required for this test program. Overall accuracy of the system is approximately 0.2%.

# 4 Test procedure

All superalloy test materials were furnished by the NASA Lewis Research Center Oxidation and Refractory Compounds Section. The material was shipped directly to the MDRL where the test model was fabricated. After each test model was shaped, physical characterization data were recorded. These included initial total weight and sample thicknesses at nine locations. The model was then instrumented with four Pt-Pt 10% Rh thermocouples, installed in the test chamber, and tested for the required number of cycles at the specified conditions of the contract. After testing, the model instrumentation was removed, and post-test photographs and weight and thickness measurements were made. Reasonable precautions were taken not to damage or contaminate the test model during these operations. The model was then suspended in a small metallic box, identified, and shipped by air express to NASA Lewis.

## 4.1 Pre-test procedure

### 4.1.1 Model preparation

Each test model was shaped to its final size of 2.95 in. x 2.95 in. (7.49 x 7.49 cm) from a 4 in. x 4 in. (10.2 x 10.2 cm) flat piece of rolled stock. The final model dimensions were established from thermal expansion calculations to minimize the gap between the sample edge and wedge holder cavity during testing. Although thermal expansion coefficients varied slightly among the five alloys tested, material expansion was never large enough to cause physical contact between the model edge and the water-cooled holder. In all cases the region between the model edge and holder cavity was filled with loosely packed Fiberfrax.

Premachined phenolic blocks with a 0.09 in. (0.23 cm) radius on the edges were used to hold the material while each model edge was bent to 90 deg (1.57 rad) forming a 0.09 in. (0.23 cm) radius bend. Prior to forming the radius, the edge regions were polished until most of the material's surface cracks were removed. This minimized the possibility of fracture during bending and resulted in smaller radii. The radii were again polished to relieve any induced stresses in the model from the bending process. Material along each folded edge was then removed by filing, except for the required tabs at midlength, until only the radius extended below the surface. This curved edge gave rigidity to the model, yet the model test surface remained effectively a flat plate. All models were fabricated so that the material rolling direction was parallel to the test stream flow direction.

After fabrication the model was placed in the wedge holder. By adjusting the pointed support screws in each quadrant of the holder, the flat model test surface was aligned in the plane of the wedge holder top surface. The model side tabs were then marked and drilled for the retaining pins.

The thermocouple attachment areas were lightly sanded to remove the thin oxide layer, and the model surfaces were thoroughly cleaned.

Pre-test thickness measurements were made at the nine positions shown in Fig. 11 using a 0.031 in. (0.079 cm) radius ball Starrett micrometer. The accuracy of the measurments was ± 0.0005 in. (0.0013 cm). The model surface was again cleaned and a pre-test weight determined on a Voland and Sons analytical balance to an accuracy of ± 0.001 g.

The Pt-Pt 10% Rh thermocouples were tack welded at the four locations shown in Fig. 11. Each wire was electrically and thermally insulated with Teflon tubing and small alumina tubing beads. Placement of the thermocouples was critical because of the high thermal gradient along the model longitudinal axis. Thermocouple numbers 2, 3 and 4, shown in Fig. 11, were referenced to the model leading edge and longitudinal centerline, whereas number 1 was referenced to the trailing edge and centerline.

### 4.1.2 Model installation

After attachment of the thermocouple and ground wires, the backface of the test model was covered with one layer of 1/4 in. (0.64 cm) thick Fiberfrax insulation blanket. The insulated thermocouples were individually fed through this layer and then bundled together. The cavity in the wedge holder was filled with three layers of Fiberfrax with the center region open to allow passage of the thermocouple wires. The thermocouple wires were completely protected in the test chamber by the water-cooled wedge holder, the model actuator arm, and the model actuator.

The test model was placed in the wedge holder and held in position by three adjustable retaining pins on the sides and one stationary pin at the leading edge. These four retaining pins maintained the model edges flush with the wedge holder surface throughout the test. Additional model support was provided in each quadrant by adjustable set screws passing through the holder backface and insulation layers. These screws were pointed to minimize the contact with the model backface.

The model holder arm was aligned so the model test surface was at 60 deg (1.05 rad) to the nozzle axis with the wedge holder leading edge vertical and 1 in. (2.54 cm) downstream of the nozzle exit plane. The test model geometric center was located on the axial centerline of the nozzle and test stream. The alignment was checked periodically to ensure that no changes had occurred.

## 4.2 Calibration

Prior to conducting the material evaluation tests, a series of calibration runs were made in the PAT facility to establish the heat flux and surface pressure profiles at the two operating conditions. The measured cold wall heat flux distribution along the 60 deg (1.05 rad) wedge test surface is shown in Fig. 12 for both test conditions. Each value repre-

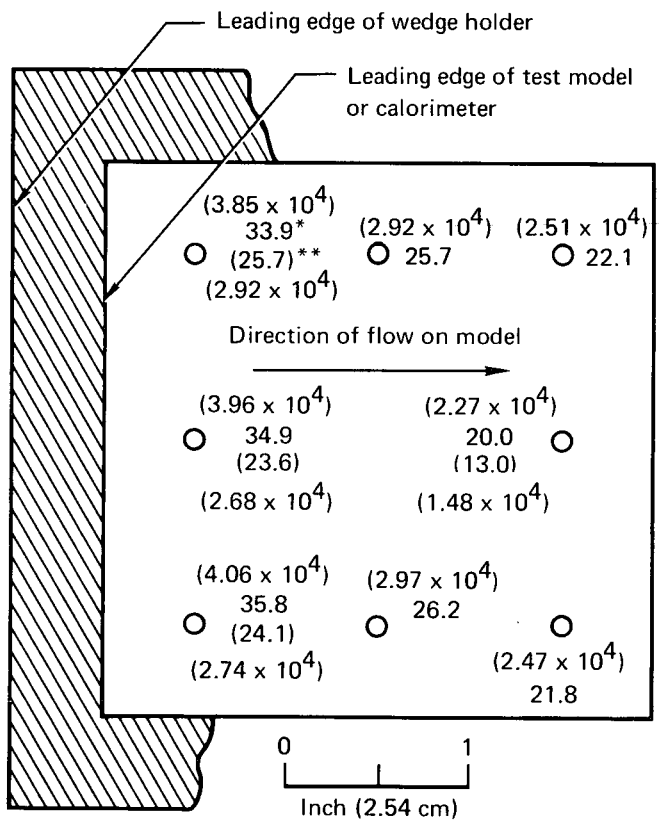


*Heat flux in Btu/ft$^2$ sec (W/m$^2$) with model temperature at 2200°F (1478 K)
**Heat flux in Btu/ft$^2$ sec (W/m$^2$) with model temperature at 2000°F (1367 K)

**Fig. 12 Cold wall heat flux distribution with model at 60 deg (1.05 rad) angle of attack**

sents an average of four data points. The numbers in parentheses were obtained for the lower test condition (2000°F (1367 K) on the model leading edge) while the other values correspond to the higher test condition (2200°F (1478 K) on the model leading edge). These values show the lateral uniformity of the flow over the model surface. The axial variation of the heat flux indicates the flow to be laminar since it varies inversely with the square root of distance.

The surface pressure distribution is shown in Fig. 13. Only one set of values is presented since the chamber pressure upstream of the nozzle throat was maintained constant at approximately 525 ± 10 Torr ($7.0 \times 10^4 \pm 1.3 \times 10^3$ N/m$^2$) for both test conditions. Other parameters which affect the surface pressure such as the nozzle area ratio, model holder angle of attack, and stream enthalpy, also remained constant. The values were measured with a 0 - 1 psid (0 - $6.9 \times 10^3$ N/m$^2$) Statham transducer with the reference pressure being the ambient pressure in the test chamber. The ambient pressure in the test chamber was constant for both test conditions at 0.68 Torr (90.7 N/m$^2$). This was achieved by individually controlling the primary and secondary air flow rates into the arc heater in the proper proportions to maintain a constant total mass flow rate.

Other heat flux and pressure calibrations have been made in the PAT facility at various conditions using the same nozzle (8 in. (20.3 cm) diam exit) as was employed for this contractual test program. Figure 14 shows some of these measurements made at three different axial positions. The measurements were normalized to the centerline values and indicate a uniform test environment within ± 10% over a 6 in. (15.2 cm) diam test core.

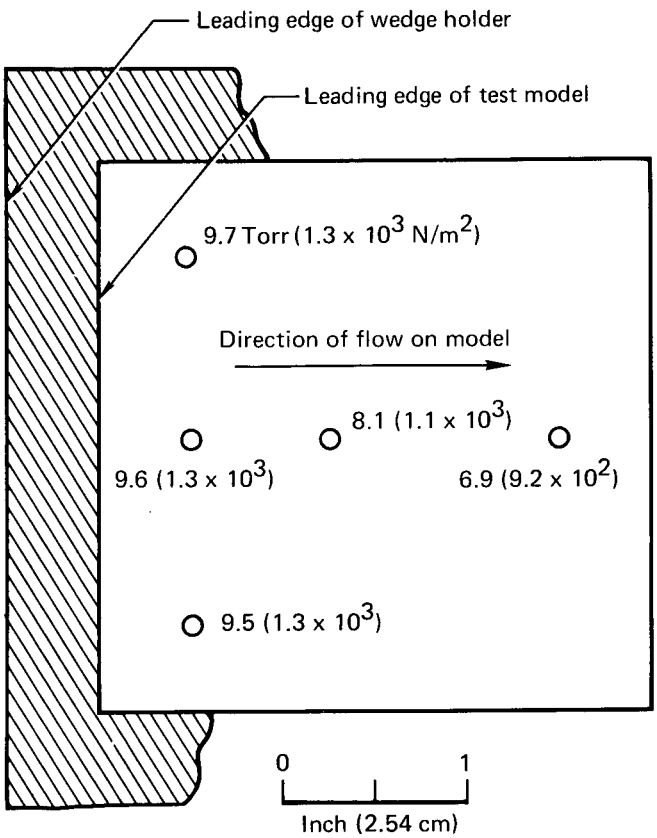


**Fig. 13 Surface pressure distribution with model at 60 deg (1.05 rad) angle of attack**

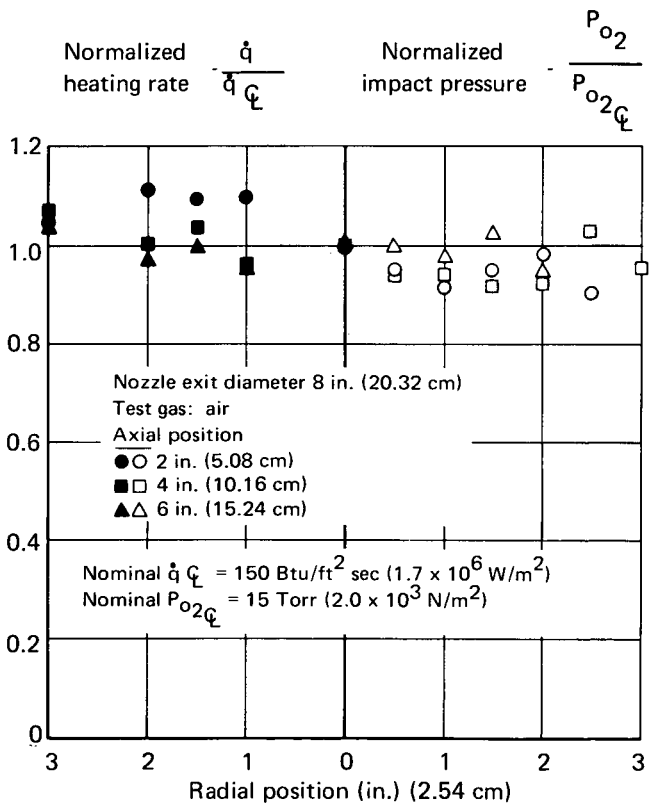


**Fig. 14 PAT facility test stream uniformity**

## 4.3 Test procedure

After a model was installed, photographs made, and the thermocouple instrumentation connected, preparations were made for a facility run. The steam ejector system used to evacuate the test chamber was activated first. All facility instrumentation was checked through the CDAS for proper calibration constants, continuity, zero shift, and balancing on bridge circuits. When this had been accomplished, the cooling water and air flow systems were energized. The test chamber was evacuated and the arc heater power supplies were turned on. A high voltage was applied across the arc heater electrodes to initiate the arc. After the arc heater was stabilized at the predetermined test condition, the model was injected into the test stream. The operating parameters were held constant while the test model was reaching an equilibrium temperature. The model temperature as measured by the thermocouples was displayed on the CDAS digital monitor unit for the test conductor's observation. The models reached a leading edge temperature of 2200°F (1478 K) in approximately 100 sec. To maintain this temperature, minute changes in the arc current and air mass flow rates were made as required during each cycle. The changes were regulated in a manner that would yield the proper model temperature while maintaining an arc heater chamber pressure ($P_o$) of 525 ± 10 Torr ($7.0 \times 10^4 \pm 1.3 \times 10^3$ N/m$^2$). Thus, the model surface pressure did not vary more than ±0.19 Torr (25.3 N/m$^2$).

At approximately the midpoint of each 10 min test cycle, a manual record of the four thermocouple outputs and the thirteen optical pyrometer temperatures was made in addition to the simultaneous permanent recording on the CDAS. During the time required to record these values, (approximately 1 min) no changes were made in the arc heater operating parameters. This procedure was established so the recorded temperatures would correspond to a given test condition.

Model test times were recorded automatically in the PAT control room. A timer was activated by insertion and removal of the model actuator arm into the test stream. In addition, a signal was recorded on the CDAS to indicate when a model was in the test stream, thus establishing the arc heater conditions during that time.

At the completion of a 10 min cycle, the model was removed from the test stream and allowed to cool radiatively to a uniform temperature of 400°F (478 K) or less. This normally required 2.5 min while the test chamber remained at a constant pressure of 0.7 Torr (93.3 N/m$^2$). The arc heater was normally operated without interruption during model cooling. Periodically, operation was stopped to permit arc heater or test model inspection.

After the model surface had cooled to 400°F (478 K) and the arc heater operating parameters were checked, the model was recycled into the test stream. Tests on each model continued in the manner described above until the required number of cycles had been completed.

Pre-test and post-test color photographs were normally taken with the model installed in the wedge holder. Post-test photographs of the model front and back surfaces were also made. During the tests additional photographs were taken to document various events.

## 4.4 Post-test procedure

After completion of all the required test cycles, the model was removed from the wedge holder. After photographing the model, the four thermocouples and ground wires were removed. While handling the model, white nylon gloves were worn to protect the model from contamination. Touching of the front and back surfaces was kept to a minimum to avoid damaging the surface oxide layers. A post-test model weight was obtained and the nine post-test thickness measurements made. The model was then suspended in a metallic container and shipped air express to NASA Lewis c/o Dr. H.B. Probst, Head, Oxidation and Refractory Compounds Section. A similar procedure was followed for all the test models.

# 5 Discussion of results

## 5.1 Tests

A total of seven models and five different materials were evaluated in this test program. The model material, test order, control temperature, and number of test cycles are given in Table III.

**Table III Test program summary**

| Model test order | Material | Control temperature | Number of cycles | Total test time (min) |
|---|---|---|---|---|
| 1 | TD-NiCr | 2200°F (1478 K) | 25 | 252 |
| 2 | TD-NiCrAlY | 2200°F (1478 K) | 25 | 250 |
| 3 | DS-NiCr | 2200°F (1478 K) | 25 | 250 |
| 4 | Haynes-188 | 2000°F (1367 K) | 25 | 250 |
| 5 | TD-NiCr | 2200°F (1478 K) | 50 | 500 |
| 6 | DS-NiCr | 2200°F (1478 K) | 50 | 500 |
| 7 | TD-NiCrAl | 2200°F (1478 K) | 25 | 250 |

Table IV summarizes the arc heater operating conditions for this test program.

**Table IV Arc heater operating conditions**

| Model number | Bulk enthalpy Btu/lb (J/kg) | Chamber pressure Torr ($N/m^2$) | Air flow rate lb/sec (kg/sec) |
|---|---|---|---|
| 1 | 2850 ($6.63 \times 10^6$) | 535 ($7.13 \times 10^4$) | 0.039 (0.018) |
| 2 | 2850 ($6.63 \times 10^6$) | 525 ($7.00 \times 10^4$) | 0.039 (0.018) |
| 3 | 2850 ($6.63 \times 10^6$) | 535 ($7.13 \times 10^4$) | 0.039 (0.018) |
| 4 | 2450 ($5.70 \times 10^6$) | 525 ($7.00 \times 10^4$) | 0.041 (0.019) |
| 5 | 2850 ($6.63 \times 10^6$) | 525 ($7.00 \times 10^4$) | 0.039 (0.018) |
| 6 | 2850 ($6.63 \times 10^6$) | 515 ($6.87 \times 10^4$) | 0.039 (0.018) |
| 7 | 2850 ($6.63 \times 10^6$) | 535 ($7.13 \times 10^4$) | 0.039 (0.018) |

The four backface thermocouple outputs were recorded at a nominal scan rate of six times per minute. This rate was increased to 60 times per minute during that portion of the cycle when model surface temperature measurements were made using the optical pyrometer. Thus, the amount of tabulated data is too voluminous to be included in the content of this report. The data will be kept on file for one year at MDRL for detailed investigation should anomalies appear during the NASA post-test material analyses.

Typical surface and backface temperatures of selected cycles are given in Tables V through XI for each model tested. The surface temperatures shown in the tables have been corrected to compensate for the difference between the calibrated and indicated temperatures from the pyrometer. A second correction was applied to remove the effect of the 1/2 in. (1.27 cm) thick quartz observation window. The transmittance value of the fused quartz window at 0.8 $\mu$m was 0.92 as determined by calibration in MCAIR Calibration Laboratory. The quartz window was protected from particle deposition on the inside surface by an air bleed system which also provided cooling. This eliminated any model temperature errors resulting from transmittance changes during a test.

The pyrometer emittance control was set at 1.0 for these tests. Since the test material emittance was not known at elevated temperatures, the true surface temperatures were not obtained. However, the data can be utilized in determining a relative distribution over the model surface.

Table V Model no. 1 (TD-NiCr) surface* and backface temperatures (°F) (K) at midpoint of test cycle

| Pyrometer sighting position (see Fig. 11) | Test cycle | | | | | |
|---|---|---|---|---|---|---|
| | 3 | 5 | 10 | 15 | 20 | 25 |
| 1 | 1962 (1346) | 1962 (1346) | 1870 (1294) | 1824 (1269) | 1859 (1288) | 1951 (1339) |
| 2 | 1996 (1364) | 1984 (1358) | 1892 (1307) | 1846 (1281) | 1859 (1288) | 1916 (1320) |
| 3 | 2037 (1387) | 2037 (1387) | 1951 (1339) | 1870 (1294) | 1881 (1301) | 1962 (1346) |
| 4 (1)** | 2058 (1399) | 2037 (1387) | 1927 (1326) | 1881 (1301) | 1881 (1301) | 1962 (1346) |
| 5 | 2105 (1425) | 2037 (1387) | 2058 (1399) | 1996 (1364) | 2017 (1376) | 2037 (1387) |
| 6 | 2104 (1424) | 2027 (1382) | 2027 (1382) | 1984 (1358) | 1937 (1332) | 1984 (1358) |
| 7 | 2213 (1485) | 2176 (1464) | 2086 (1414) | 2048 (1393) | 2037 (1387) | 2048 (1393) |
| 8 (3) | 2241 (1500) | 2150 (1450) | 2123 (1435) | 2067 (1404) | 2067 (1404) | 2048 (1393) |
| 9 (4) | 2270 (1517) | 2213 (1485) | 2204 (1480) | 2132 (1440) | 2222 (1490) | 2067 (1404) |
| 10 | 2280 (1522) | 2231 (1495) | 2195 (1475) | 2132 (1440) | 2195 (1475) | – – |
| 11 | 2301 (1534) | 2251 (1506) | 2195 (1475) | 2159 (1455) | 2213 (1485) | 2150 (1450) |
| 12 | 2312 (1540) | 2270 (1517) | 2222 (1490) | 2185 (1469) | 2231 (1495) | 2185 (1469) |
| 13 (2) | 2280 (1522) | 2251 (1506) | 2195 (1475) | 2159 (1455) | 2222 (1490) | 2222 (1490) |
| Backface thermocouple position | | | | | | |
| 1 | – – | 2022 (1379) | 1982 (1357) | 1979 (1355) | – – | 1984 (1358) |
| 2 | – – | 2211 (1484) | 2203 (1479) | 2197 (1476) | – – | 2218 (1488) |
| 3 | – – | 2190 (1472) | 2149 (1449) | 2140 (1444) | 2104 (1424) | 2091 (1417) |
| 4 | – – | 2203 (1479) | 2221 (1489) | 2221 (1489) | 2218 (1488) | 2198 (1477) |

Table VI Model no. 2 (TD-NiCrAlY) surface* and backface temperatures (°F) (K) at midpoint of test cycle

| Pyrometer sighting position (see Fig. 11) | Test cycle | | | | | |
|---|---|---|---|---|---|---|
| | 1 | 5 | 10 | 15 | 20 | 25 |
| 1 | 2006 (1370) | 1945 (1336) | 1872 (1296) | 1945 (1336) | 1870 (1294) | 1909 (1316) |
| 2 | 2006 (1370) | 1951 (1339) | 1878 (1299) | 1945 (1336) | 1870 (1294) | 1905 (1314) |
| 3 | 2006 (1370) | 1973 (1352) | 1909 (1316) | 1965 (1347) | 1909 (1316) | 1939 (1333) |
| 4 (1)** | 2017 (1376) | 1962 (1346) | 1905 (1314) | 1973 (1352) | 1909 (1316) | 1945 (1342) |
| 5 | 2100 (1422) | 2042 (1390) | 1996 (1364) | 2042 (1390) | 2006 (1370) | 2027 (1382) |
| 6 | 2093 (1418) | 2027 (1382) | 1975 (1353) | 2021 (1378) | 1996 (1364) | 2017 (1376) |
| 7 | 2086 (1414) | 2037 (1357) | 1984 (1358) | 2062 (1401) | 2027 (1382) | 2042 (1390) |
| 8 (3) | 2114 (1430) | 2077 (1409) | 2062 (1401) | 2108 (1427) | 2048 (1393) | 2093 (1418) |
| 9 (4) | 2204 (1480) | 2174 (1463) | 2066 (1403) | 2168 (1460) | 2168 (1460) | 2195 (1475) |
| 10 | 2204 (1480) | 2176 (1464) | 2168 (1460) | 2179 (1466) | 2195 (1475) | 2213 (1485) |
| 11 | 2195 (1475) | 2176 (1464) | 2159 (1455) | 2179 (1466) | 2185 (1469) | 2213 (1485) |
| 12 | 2185 (1469) | 2168 (1460) | 2150 (1450) | 2168 (1460) | 2190 (1472) | 2200 (1478) |
| 13 (2) | 2172 (1462) | 2159 (1455) | 2164 (1458) | 2179 (1466) | 2172 (1462) | 2195 (1475) |
| Backface thermocouple position | | | | | | |
| 1 | 1975 (1353) | 1932 (1329) | 1896 (1309) | 1917 (1321) | 1893 (1307) | 1902 (1312) |
| 2 | 2151 (1450) | 2157 (1454) | 2148 (1449) | 2157 (1454) | 2145 (1447) | 2145 (1447) |
| 3 | 2111 (1428) | 2090 (1417) | 2069 (1405) | 2084 (1413) | 2067 (1404) | 2072 (1407) |
| 4 | 2201 (1478) | 2205 (1481) | 2214 (1486) | 2211 (1484) | 2208 (1482) | 2213 (1485) |

Note: * Pyrometer temperatures have been corrected for calibration effect and observation window transmittance. All temperatures were obtained with pyrometer emittance control set at 1.0.
** Thermocouple number that corresponds to this pyrometer sighting position. (see Fig. 11).

Table VII Model no. 3 (DS-NiCr) surface* and backface temperatures (°F) (K) at midpoint of test cycle

| Pyrometer sighting position (see Fig. 11) | Test cycle | | | | | |
|---|---|---|---|---|---|---|
| | 2 | 5 | 10 | 15 | 20 | 25 |
| 1 | 1985 (1358) | 1911 (1317) | 1845 (1281) | 1850 (1283) | 1845 (1281) | 1835 (1275) |
| 2 | 1995 (1364) | 1911 (1317) | 1858 (1288) | 1850 (1283) | 1820 (1267) | 1835 (1275) |
| 3 | 2015 (1375) | 1925 (1325) | 1902 (1312) | 1890 (1306) | 1858 (1288) | 1870 (1294) |
| 4 (1)** | 2025 (1381) | 1960 (1344) | 1913 (1318) | 1921 (1323) | 1870 (1294) | 1915 (1349) |
| 5 | 2140 (1444) | 2092 (1418) | 2092 (1418) | 2052 (1396) | 1980 (1356) | 2050 (1394) |
| 6 | 2086 (1414) | 2048 (1393) | 2005 (1369) | 2030 (1383) | 1980 (1356) | 2005 (1369) |
| 7 | 2231 (1495) | 2120 (1433) | 2072 (1407) | 1992 (1362) | 2088 (1416) | 2090 (1417) |
| 8 (3) | 2250 (1506) | 2155 (1453) | 2140 (1444) | 2130 (1439) | 2140 (1444) | 2090 (1417) |
| 9 (4) | 2290 (1528) | 2275 (1519) | 2250 (1506) | 2130 (1439) | 2185 (1469) | 2185 (1469) |
| 10 | 2296 (1528) | 2291 (1528) | 2238 (1499) | 2238 (1499) | 2220 (1489) | 2200 (1478) |
| 11 | 2306 (1537) | 2275 (1519) | 2230 (1494) | 2238 (1499) | 2220 (1489) | 2215 (1486) |
| 12 | 2306 (1537) | 2278 (1521) | 2258 (1510) | 2243 (1502) | 2220 (1489) | 2215 (1486) |
| 13 (2) | 2306 (1537) | 2270 (1517) | 2258 (1510) | 2255 (1508) | 2221 (1489) | 2185 (1469) |
| Backface thermocouple position | | | | | | |
| 1 | 1963 (1346) | 1909 (1316) | 1875 (1297) | 1899 (1310) | 1916 (1320) | 1917 (1321) |
| 2 | 2195 (1475) | 2218 (1488) | 2204 (1480) | 2218 (1488) | 2211 (1484) | 2205 (1481) |
| 3 | 2109 (1427) | 2100 (1422) | 2271 (1517) | 2097 (1421) | 2101 (1423) | 2101 (1473) |
| 4 | 2191 (1493) | 2227 (1486) | 2215 (1481) | 2206 (1477) | 2199 (1472) | 2189 (1257) |

Table VIII Model no. 4 (Haynes 188) surface* and backface temperatures (°F) (K) at midpoint of test cycle

| Pyrometer sighting position (see Fig. 11) | Test cycle | | | | | |
|---|---|---|---|---|---|---|
| | 1 | 5 | 10 | 15 | 20 | 25 |
| 1 | — — | — — | — — | — — | — — | — — |
| 2 | — — | — — | — — | — — | — — | — — |
| 3 | — — | — — | — — | — — | 1803 (1257) | 1780 (1244) |
| 4 (1)** | — — | — — | — — | — — | 1803 (1257) | 1803 (1257) |
| 5 | 1888 (1304) | 1881 (1301) | — — | 1853 (1285) | 1870 (1294) | 1859 (1288) |
| 6 | 1870 (1294) | 1881 (1301) | — — | 1837 (1276) | 1873 (1296) | 1859 (1288) |
| 7 | 1955 (1342) | 1962 (1346) | 1803 (1257) | 1909 (1316) | 1951 (1339) | 1939 (1333) |
| 8 (3) | 1975 (1353) | 1962 (1346) | 1846 (1281) | 1962 (1346) | 1951 (1339) | 1951 (1339) |
| 9 (4) | 2017 (1376) | 2052 (1396) | 1936 (1331) | 2006 (1370) | 2017 (1376) | 2006 (1370) |
| 10 | 2021 (1378) | 2048 (1393) | 1962 (1346) | 2037 (1387) | 2058 (1399) | 2037 (1387) |
| 11 | 2027 (1382) | 2037 (1387) | 1955 (1342) | 2037 (1387) | 2067 (1404) | 2048 (1393) |
| 12 | 2031 (1384) | 2058 (1399) | 1984 (1358) | 2037 (1387) | 2087 (1415) | 2058 (1399) |
| 13 (2) | 2037 (1387) | 2048 (1393) | 1962 (1346) | 2027 (1382) | 2058 (1399) | 2058 (1399) |
| Backface thermocouple position | | | | | | |
| 1 | 1729 (1216) | 1769 (1238) | 1742 (1223) | 1782 (1246) | 1794 (1252) | 1791 (1251) |
| 2 | 1975 (1353) | 2007 (1371) | 1986 (1359) | 1999 (1366) | 2012 (1373) | 2003 (1368) |
| 3 | 1895 (1308) | 1927 (1326) | 1909 (1316) | 1933 (1329) | 1939 (1333) | 1933 (1329) |
| 4 | 1968 (1349) | 1989 (1361) | 1981 (1356) | 1994 (1363) | 1982 (1357) | 1972 (1351) |

Note: * Pyrometer temperatures have been corrected for calibration effect and observation window transmittance. All temperatures were obtained with pyrometer emittance control set at 1.0.

** Thermocouple number that corresponds to this pyrometer sighting position. (see Fig. 11).

Table IXa Model no. 5 (TD-NiCr) surface* and backface temperatures (°F) (K) at midpoint of test cycle

| Pyrometer sighting position (see Fig. 11) | Test Cycle | | | | | |
|---|---|---|---|---|---|---|
| | 1 | 5 | 10 | 15 | 20 | 25 |
| 1 | 2017 (1376) | 1892 (1307) | 1881 (1301) | 1892 (1307) | 1866 (1292) | 1899 (1310) |
| 2 | 2017 (1376) | 1892 (1307) | 1837 (1276) | 1881 (1301) | 1892 (1307) | 1899 (1384) |
| 3 | 2031 (1384) | 1929 (1327) | 1919 (1322) | 1909 (1316) | 1939 (1333) | 1916 (1320) |
| 4 (1)** | 2037 (1387) | 1962 (1346) | 1919 (1322) | 1939 (1333) | 1955 (1342) | 1945 (1336) |
| 5 | 2128 (1438) | 2077 (1409) | 2048 (1393) | 2021 (1378) | 2017 (1376) | 2001 (1367) |
| 6 | 2082 (1412) | 2037 (1387) | 1990 (1361) | 1984 (1358) | 2096 (1420) | 1984 (1358) |
| 7 | 2132 (1440) | 2086 (1414) | 2042 (1390) | 2067 (1404) | 2067 (1404) | 2017 (1376) |
| 8 (3) | 2185 (1469) | 2118 (1432) | 2077 (1409) | 2096 (1420) | 2217 (1487) | 2052 (1396) |
| 9 (4) | – | 2231 (1495) | 2222 (1490) | 2213 (1485) | 2235 (1497) | 2222 (1490) |
| 10 | 2311 (1539) | 2120 (1433) | 2204 (1480) | 2209 (1483) | 2222 (1490) | 2213 (1485) |
| 11 | 2291 (1528) | 2222 (1490) | 2195 (1475) | 2222 (1490) | 2204 (1480) | 2204 (1480) |
| 12 | 2291 (1528) | 2222 (1490) | 2204 (1480) | 2204 (1480) | 2222 (1490) | 2205 (1481) |
| 13 (2) | 2291 (1528) | 2222 (1490) | 2204 (1480) | 2185 (1469) | 2195 (1475) | 2195 (1475) |
| **Backface thermocouple position** | | | | | | |
| 1 | 1995 (1364) | 1901 (1312) | 1889 (1305) | 1903 (1313) | 1893 (1307) | 1916 (1320) |
| 2 | 2179 (1466) | 2200 (1478) | 2184 (1469) | 2180 (1467) | 2173 (1463) | 2195 (1475) |
| 3 | 2108 (1427) | 2080 (1411) | 2061 (1401) | 2045 (1392) | 2032 (1384) | 2052 (1396) |
| 4 | 2219 (1488) | 2199 (1475) | 2208 (1482) | 2201 (1478) | 2190 (1472) | 2208 (1482) |

Table IXb Model no. 5 (TD-NiCr) surface* and backface temperatures (°F) (K) at midpoint of test cycle

| Pyrometer sighting position (see Fig. 11) | Test cycle | | | | |
|---|---|---|---|---|---|
| | 30 | 35 | 40 | 45 | 50 |
| 1 | 1939 (1333) | 1945 (1336) | 1905 (1314) | 1905 (1314) | 1881 (1301) |
| 2 | 1939 (1333) | 1951 (1339) | 1916 (1320) | 1916 (1320) | 1881 (1301) |
| 3 | 1962 (1346) | 1951 (1339) | 1945 (1336) | 1939 (1333) | 1909 (1316) |
| 4 (1)** | 1984 (1358) | 1962 (1346) | 1965 (1347) | 1984 (1358) | 1973 (1352) |
| 5 | 2048 (1393) | 1984 (1358) | 2011 (1373) | 2027 (1382) | 2048 (1393) |
| 6 | 2027 (1382) | 2037 (1387) | 2011 (1373) | 2017 (1376) | 2048 (1393) |
| 7 | 2067 (1404) | 2017 (1376) | 2031 (1384) | 2037 (1387) | 2067 (1404) |
| 8 (3) | 2086 (1414) | 2058 (1399) | 2128 (1438) | 2123 (1435) | 2096 (1420) |
| 9 (4) | 2307 (1537) | 2301 (1534) | 2241 (1501) | 2256 (1509) | 2231 (1495) |
| 10 | 2280 (1522) | 2342 (1557) | 2256 (1509) | 2251 (1506) | 2246 (1503) |
| 11 | 2260 (1511) | 2331 (1550) | 2246 (1503) | 2241 (1501) | 2251 (1506) |
| 12 | 2270 (1517) | 2331 (1551) | 2235 (1497) | 2241 (1501) | 2251 (1506) |
| 13 (2) | 2231 (1495) | 2291 (1528) | 2225 (1492) | 2231 (1495) | 2235 (1497) |
| **Backface thermocouple position** | | | | | |
| 1 | 1907 (1315) | 1904 (1313) | 1910 (1316) | 1908 (1316) | 1898 (1310) |
| 2 | 2201 (1478) | 2212 (1484) | 2216 (1487) | 2201 (1478) | 2203 (1479) |
| 3 | 2051 (1395) | 2061 (1401) | 2070 (1406) | 2055 (1397) | 2056 (1398) |
| 4 | 2199 (1477) | 2204 (1480) | 2190 (1472) | 2187 (1471) | 2188 (1471) |

Note: * Pyrometer temperatures have been corrected for calibration effect and observation window transmittance. All temperatures were obtained with pyrometer emittance control set at 1.0.

** Thermocouple number that corresponds to this pyrometer sighting position. (see Fig. 11).

Table Xa Model no. 6 (DS-NiCr) surface* and backface temperatures (°F) (K) at midpoint of test cycle

| Pyrometer sighting position (see Fig. 11) | Test cycle | | | | | |
|---|---|---|---|---|---|---|
| | 3 | 8 | 13 | 16 | 20 | 25 |
| 1 | 1940 (1333) | — — | 1927 (1326) | 1962 (1346) | 1870 (1294) | 1899 (1311) |
| 2 | 1928 (1327) | — — | 1929 (1327) | 1962 (1346) | 1870 (1294) | 1892 (1307) |
| 3 | 1962 (1346) | — — | 1962 (1346) | 1984 (1358) | 1892 (1307) | 1927 (1326) |
| 4 (1)** | 1951 (1339) | 1962 (1346) | 1962 (1346) | 1996 (1364) | 1916 (1320) | 1951 (1339) |
| 5 | 2078 (1410) | — — | 2052 (1396) | 2048 (1393) | 2048 (1393) | 2048 (1393) |
| 6 | 2006 (1370) | — — | 2029 (1383) | 2027 (1382) | 2006 (1370) | 2013 (1374) |
| 7 | 2052 (1396) | — — | 2067 (1404) | 2058 (1399) | 2037 (1387) | 2037 (1387) |
| 8 (3) | 2142 (1446) | 2096 (1420) | 2072 (1407) | 2105 (1425) | 2048 (1393) | 2067 (1404) |
| 9 (4) | 2260 (1511) | 2297 (1532) | 2231 (1495) | 2280 (1522) | 2222 (1490) | 2200 (1478) |
| 10 | 2260 (1511) | 2231 (1495) | 2176 (1464) | 2301 (1534) | 2190 (1472) | 2176 (1464) |
| 11 | 2291 (1528) | 2235 (1497) | 2204 (1480) | 2270 (1517) | 2185 (1469) | 2185 (1469) |
| 12 | 2312 (1540) | 2231 (1495) | 2222 (1490) | 2270 (1517) | 2185 (1469) | 2185 (1469) |
| 13 (2) | 2301 (1534) | 2260 (1511) | 2222 (1490) | 2204 (1480) | 2176 (1464) | 2176 (1464) |
| Backface thermocouple position | | | | | | |
| 1 | 1899 (1311) | 1852 (1284) | 1914 (1319) | 1935 (1331) | 1868 (1293) | 1911 (1317) |
| 2 | 2148 (1449) | 2121 (1434) | 2199 (1477) | 2185 (1469) | 2152 (1451) | 2188 (1471) |
| 3 | 2064 (1402) | 2043 (1391) | 2062 (1401) | 2079 (1411) | 2025 (1381) | 2052 (1396) |
| 4 | 2196 (1476) | 2175 (1464) | 2178 (1466) | 2213 (1485) | 2165 (1458) | 2190 (1472) |

Table Xb Model no. 6 (DS-NiCr) surface* and backface temperatures (°F) (K) at midpoint of test cycle

| Pyrometer sighting position (see Fig. 11) | Test cycle | | | | |
|---|---|---|---|---|---|
| | 30 | 35 | 39 | 44 | 49 |
| 1 | 1892 (1307) | 1927 (1326) | 1888 (1304) | 1881 (1301) | 1892 (1307) |
| 2 | 1905 (1314) | 1927 (1326) | 1881 (1301) | 1881 (1301) | 1881 (1301) |
| 3 | 1951 (1339) | 1951 (1339) | 1916 (1320) | 1927 (1326) | 1927 (1326) |
| 4 (1)** | 1973 (1352) | 1939 (1333) | 1939 (1333) | 1939 (1333) | 1939 (1333) |
| 5 | 2048 (1393) | 2058 (1399) | 2017 (1376) | 2017 (1376) | 2017 (1376) |
| 6 | 2058 (1399) | 2017 (1376) | 1980 (1356) | 1984 (1358) | 2017 (1376) |
| 7 | 2048 (1393) | 2048 (1393) | 2021 (1378) | 2017 (1376) | 2058 (1399) |
| 8 (3) | 2062 (1401) | 2062 (1401) | 2067 (1404) | 2077 (1409) | 2123 (1435) |
| 9 (4) | 2231 (1495) | 2231 (1495) | 2235 (1497) | 2231 (1495) | 2241 (1501) |
| 10 | 2222 (1490) | 2176 (1464) | 2190 (1472) | 2176 (1464) | 2185 (1469) |
| 11 | 2231 (1495) | 2176 (1464) | 2176 (1464) | 2168 (1460) | 2176 (1464) |
| 12 | 2195 (1475) | 2159 (1455) | 2168 (1460) | 2159 (1455) | 2176 (1464) |
| 13 (2) | 2176 (1464) | 2176 (1464) | 2174 (1463) | 2176 (1464) | 2185 (1469) |
| Backface thermocouple position | | | | | |
| 1 | 1908 (1316) | 1916 (1320) | 1896 (1309) | 1890 (1306) | 1896 (1309) |
| 2 | 2187 (1471) | 2193 (1474) | 2190 (1472) | 2184 (1469) | 2187 (1471) |
| 3 | 2046 (1392) | 2052 (1396) | 2034 (1386) | 2031 (1384) | 2027 (1382) |
| 4 | 2180 (1467) | 2182 (1468) | 2174 (1463) | 2180 (1467) | 2188 (1471) |

Note: * Pyrometer temperatures have been corrected for calibration effect and observation window transmittance. All temperatures were obtained with pyrometer emittance control set at 1.0.

** Thermocouple number that corresponds to this pyrometer sighting position. (see Fig. 11).

**Table XI Model no. 7 (TD-NiCrAℓ) surface* and backface temperatures (°F) (K) at midpoint of test cycle**

| Pyrometer sighting position (see Fig. 11) | Test cycle | | | | | |
|---|---|---|---|---|---|---|
| | 3 | 5 | 10 | 15 | 20 | 25 |
| 1 | 1946 (1337) | – – | 1835 (1275) | 1892 (1307) | 1878 (1299) | 1859 (1288) |
| 2 | 1946 (1337) | – – | 1835 (1275) | 1881 (1301) | 1835 (1275) | 1827 (1271) |
| 3 | 1965 (1347) | 1863 (1291) | 1846 (1281) | 1909 (1316) | 1859 (1288) | 1835 (1275) |
| 4 (1)** | 1962 (1346) | 1859 (1233) | 1863 (1290) | 1927 (1326) | 1899 (1310) | 1881 (1301) |
| 5 | 2087 (1415) | 2021 (1378) | 2021 (1378) | 2077 (1409) | 2042 (1390) | 2098 (1421) |
| 6 | 2031 (1384) | 1955 (1342) | 1973 (1352) | 2001 (1367) | 1984 (1358) | 1996 (1364) |
| 7 | 2072 (1407) | 2006 (1370) | 1954 (1341) | 2006 (1370) | 1990 (1361) | 1996 (1364) |
| 8 (3) | 2132 (1440) | 2021 (1378) | 2042 (1390) | 2077 (1409) | 2048 (1393) | 2096 (1420) |
| 9 (4) | 2213 (1485) | 2204 (1480) | 2225 (1492) | 2251 (1506) | 2246 (1503) | 2235 (1497) |
| 10 | 2195 (1475) | 2150 (1450) | 2218 (1488) | 2270 (1517) | 2276 (1520) | 2251 (1506) |
| 11 | 2176 (1464) | 2118 (1432) | 2200 (1478) | 2235 (1497) | 2241 (1500) | 2204 (1480) |
| 12 | 2159 (1455) | 2108 (1421) | 2159 (1455) | 2200 (1478) | 2195 (1475) | 2168 (1460) |
| 13 (2) | 2176 (1464) | 2128 (1438) | 2128 (1438) | 2246 (1503) | 2150 (1450) | 2114 (1430) |
| **Backface thermocouple position** | | | | | | |
| 1 | 1905 (1314) | 1831 (1273) | 1827 (1271) | 1848 (1282) | 1851 (1284) | 1821 (1267) |
| 2 | 2160 (1456) | 2124 (1435) | 2061 (1401) | 2145 (1447) | 2100 (1422) | 2085 (1414) |
| 3 | 2082 (1412) | 1990 (1361) | 1995 (1364) | 2023 (1379) | 2037 (1387) | 2031 (1384) |
| 4 | 2203 (1479) | 2203 (1479) | 2223 (1491) | 2263 (1513) | 2259 (1511) | 2259 (1511) |

Note: * Pyrometer temperatures have been corrected for calibration effect and observation window transmittance. All temperatures were obtained with pyrometer emittance control set at 1.0.
** Thermocouple number that corresponds to this pyrometer sighting position. (see Fig. 11).

A typical temperature profile along the model centerline from leading to trailing edge is shown in Fig. 15. As might be expected, the curve shape is similar to the heat flux profile shown in Fig. 10. There are edge losses with corresponding temperature decreases, so the curve cannot be extrapolated to a much higher temperature at the model leading edge.

Table XII gives the average and maximum temperatures measured at each pyrometer target location during the total 25 or 50 cycles for each model. As shown in Fig. 11 the pyrometer target locations numbered 1 through 3 are at the same axial distance from the nozzle exit plane. Likewise, pyrometer target locations 5 through 7 are at the same axial distance and pyrometer target locations 9 through 13 are at the same axial distance.

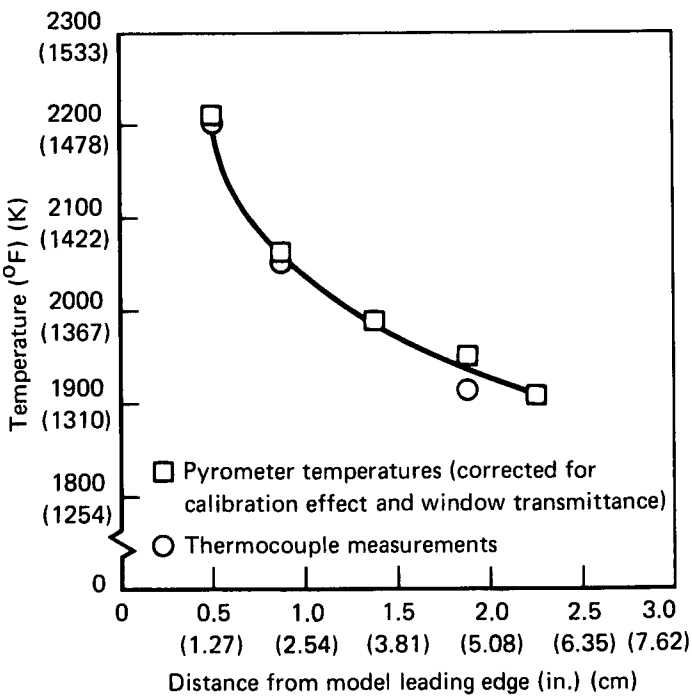


**Fig. 15 Centerline temperature profile for model no. 5 (TD-NiCr) during 25th cycle**

## Table XII Measured model temperatures using optical pyrometer

| Model description and (number of cycles) | | | | Pyrometer target locations | | | | | | | | | | | | |
|---|---|---|---|---|---|---|---|---|---|---|---|---|---|---|---|---|
| | | | | 1 | 2 | 3 | 4 | 5 | 6 | 7 | 8 | 9 | 10 | 11 | 12 | 13 |
| TD-NiCr | (25) | Ave. | (°F) | 1887 | 1895 | 2014 | 1934 | 2023 | 1993 | 2081 | 2099 | 2195 | 2186 | 2191 | 2218 | 2205 |
| | | | (K) | 1304 | 1308 | 1374 | 1330 | 1379 | 1363 | 1412 | 1422 | 1475 | 1470 | 1473 | 1488 | 1481 |
| | | Max. | (°F) | 1994 | 1994 | 2046 | 2056 | 2103 | 2122 | 2230 | 2239 | 2268 | 2279 | 2299 | 2310 | 2279 |
| | | | (K) | 1363 | 1363 | 1392 | 1398 | 1424 | 1434 | 1494 | 1499 | 1516 | 1522 | 1533 | 1538 | 1522 |
| TD-NiCrAlY | (25) | Ave. | (°F) | 1910 | 1910 | 1941 | 1947 | 2028 | 2013 | 2026 | 2083 | 2187 | 2194 | 2189 | 2182 | 2176 |
| | | | (K) | 1317 | 1317 | 1334 | 1337 | 1382 | 1374 | 1381 | 1413 | 1471 | 1474 | 1472 | 1468 | 1464 |
| | | Max. | (°F) | 2004 | 2004 | 2004 | 2016 | 2098 | 2091 | 2085 | 2116 | 2220 | 2230 | 2230 | 2230 | 2215 |
| | | | (K) | 1369 | 1369 | 1369 | 1376 | 1421 | 1417 | 1414 | 1431 | 1489 | 1494 | 1494 | 1494 | 1486 |
| DS-NiCr | (25) | Ave. | (°F) | 1880 | 1863 | 1913 | 1939 | 2072 | 2045 | 2116 | 2161 | 2252 | 2135 | 2263 | 2263 | 2262 |
| | | | (K) | 1300 | 1291 | 1318 | 1333 | 1407 | 1392 | 1431 | 1456 | 1507 | 1442 | 1513 | 1513 | 1512 |
| | | Max. | (°F) | 1983 | 1994 | 2015 | 2026 | 2140 | 2094 | 2230 | 2249 | 2289 | 2295 | 2305 | 2305 | 2305 |
| | | | (K) | 1357 | 1363 | 1375 | 1381 | 1444 | 1419 | 1494 | 1505 | 1527 | 1531 | 1536 | 1536 | 1536 |
| Haynes-188 | (25) | Ave. | (°F) | * | * | * | * | 1861 | 1862 | 1936 | 1912 | 2013 | 2037 | 2043 | 2002 | 2041 |
| | | | (K) | * | * | * | * | 1289 | 1290 | 1331 | 1318 | 1374 | 1387 | 1391 | 1368 | 1389 |
| | | Max. | (°F) | * | * | * | * | 1914 | 1994 | 1972 | 1979 | 2066 | 2076 | 2076 | 2081 | 2066 |
| | | | (K) | * | * | * | * | 1319 | 1363 | 1351 | 1355 | 1403 | 1409 | 1409 | 1412 | 1403 |
| TD-NiCr | (50) | Ave. | (°F) | 1912 | 1912 | 1930 | 1964 | 1942 | 2027 | 2055 | 2110 | 2244 | 2248 | 2240 | 2241 | 2224 |
| | | | (K) | 1318 | 1318 | 1328 | 1347 | 1334 | 1382 | 1397 | 1428 | 1502 | 1504 | 1500 | 1500 | 1491 |
| | | Max. | (°F | 2016 | 2016 | 2030 | 2036 | 2127 | 2094 | 2131 | 2215 | 2305 | 2340 | 2330 | 2319 | 2289 |
| | | | (K) | 1376 | 1376 | 1383 | 1387 | 1437 | 1419 | 1439 | 1486 | 1536 | 1555 | 1550 | 1544 | 1527 |
| DS-NiCr | (50) | Ave. | (°F) | 1906 | 1904 | 1938 | 1952 | 2042 | 2010 | 2043 | 2081 | 2235 | 2203 | 2203 | 2201 | 2195 |
| | | | (K) | 1314 | 1313 | 1332 | 1340 | 1390 | 1372 | 1391 | 1412 | 1497 | 1479 | 1479 | 1478 | 1475 |
| | | Max. | (°F) | 1960 | 1960 | 1983 | 1994 | 2076 | 2026 | 2066 | 2140 | 2279 | 2299 | 2289 | 2309 | 2299 |
| | | | (K) | 1344 | 1344 | 1357 | 1363 | 1409 | 1381 | 1403 | 1444 | 1522 | 1533 | 1527 | 1538 | 1533 |
| TD-NiCrAl | (25) | Ave. | (°F) | 1880 | 1864 | 1878 | 1896 | 2055 | 1988 | 2002 | 2068 | 2227 | 2225 | 2194 | 2162 | 2155 |
| | | | (K) | 1300 | 1291 | 1299 | 1307 | 1397 | 1360 | 1368 | 1404 | 1493 | 1492 | 1474 | 1457 | 1453 |
| | | Max. | (°F) | 1944 | 1944 | 1964 | 1960 | 2086 | 2030 | 2071 | 2131 | 2249 | 2275 | 2239 | 2198 | 2244 |
| | | | (K) | 1336 | 1336 | 1347 | 1344 | 1414 | 1383 | 1406 | 1439 | 1505 | 1286 | 1499 | 1476 | 1502 |

*Temperature too low to measure with optical pyrometer.

Figure 16 shows for each model the nominal temperature distribution along the model as measured by the optical pyrometer. The plotted data are the average values shown in Table XII. Where there was more than one pyrometer target location at a given axial distance, an average value was plotted.

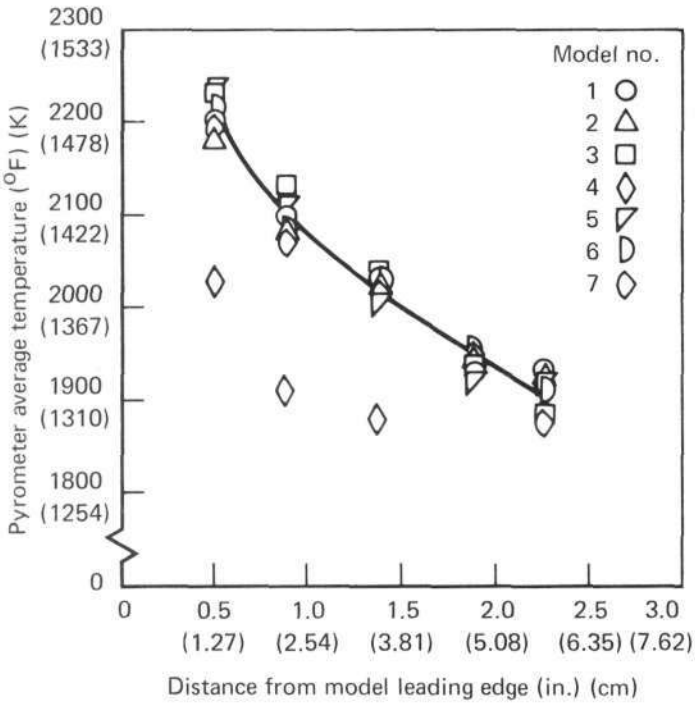


**Fig. 16 Model average temperature profile**

An AGA Thermovision Model 680 infrared camera was used to determine the qualitative temperature distribution on a MDC supplied TD-NiCr sample. This camera utilizes the temperature dependent infrared radiation from the surface of an object and displays the resultant temperature in the form of a thermogram. Five isotherms were arbitrarily selected and photographed in sequence during the test cycle. The resulting composite photograph of these isotherms is shown in Fig. 17. The horizontal dimension is distorted since the sample was at 60 deg (1.05 rad) angle of attack. Discounting edge effects, it is evident from Fig. 17 that a uniform temperature distribution occurred in the vertical direction over most of the sample test surface.

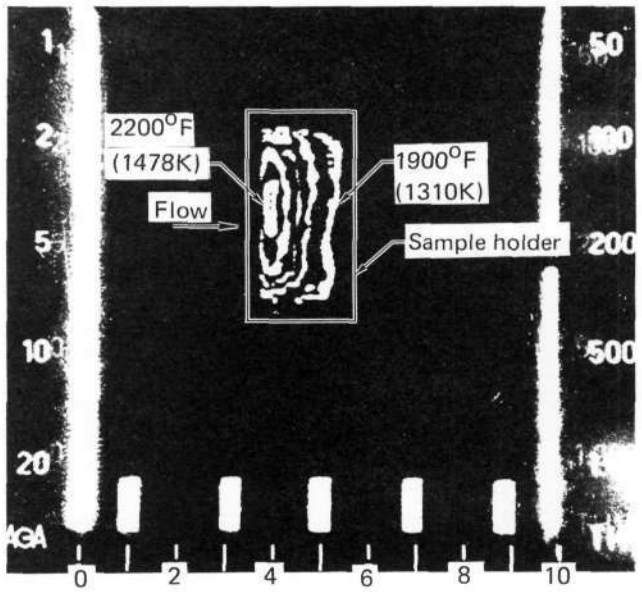


Notes:

- 3 x 3 in. (7.6 x 7.6 cm) sample
- 60 deg (1.05 rad) angle of attack
- PAT facility

**Fig. 17 Isotherms on TD-NiCr sample during test**

An 88 node thermal model was established for a computer program to calculate the effects of the thermocouple attachments on the backface temperature measurements. It was determined that conduction and radiation losses from the thermocouple wires would only affect the thermocouple measurements by $\pm 6^{\circ}$F ($\pm 3.3$ K).

A typical temperature history illustrating material response is plotted in Fig. 18. The data for the curves were obtained during the 25th cycle of NASA test model No. 5 (TD-NiCr). The final equilibrium temperature of 2200°F (1478 K) was attained in approximately 100 sec which was typical for all tests. This response occurred while the arc heater parameters and stream conditions remained constant at the predetermined values. The symbols represent data from the two leading edge thermocouples and show their spread to be less than 20°F (11 K) with the absolute measurements within $\pm 15^{\circ}$ (8.3 K) of 2200°F (1478 K). At the cycle termination (600 sec) when the model was removed from the airstream, the temperatures decreased abruptly

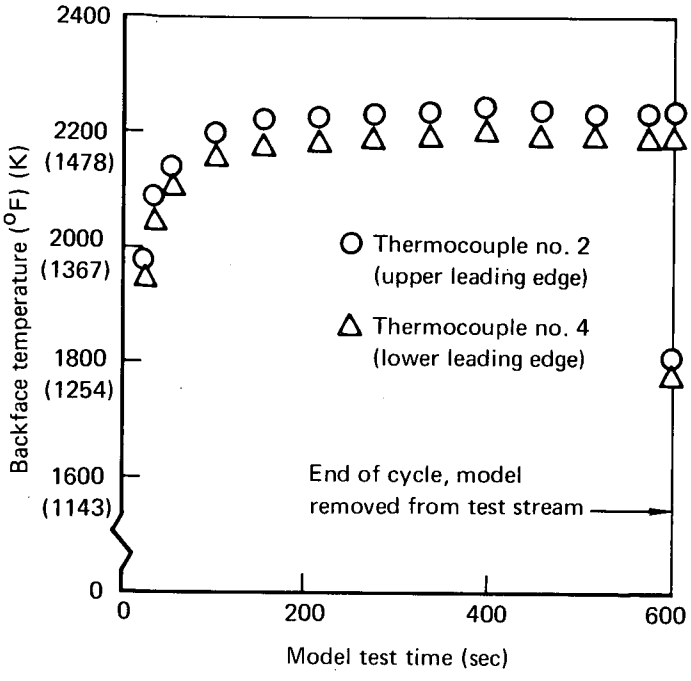


**Fig. 18 Model no. 5 (TD-NiCr) temperature response (25th cycle) 0.5 in. (1.72 cm) from model leading edge**

to approximately 1500°F (1089 K) in 10 sec. The total time required for cooling of the model to 400°F (477 K) or less required 2 to 3 min.

The temperature spread of 20°F (11 K) between the two leading edge thermocouples was typical of all model test cycles except the TD-NiCrAl and TD-NiCrAlY models. During these tests it was impossible to maintain this differential. Model No. 2 was therefore cycled maintaining thermocouple No. 4 at 2200 ± 20°F (1478 ± 11 K). Model No. 7 was cycled maintaining the average of thermocouple Nos. 2 and 4 at 2200 ± 20°F (1478 ± 11 K).

More difficulty was encountered in fabricating Model Nos. 2 and 7 than in the other models. The material was more susceptible to cracking at a bend, and thus the edge radii on these models were slightly larger than on the other models. As a result the gap (for thermal expansion of the model) between the model and wedge model holder was filled with slightly more Fiberfrax on Model Nos. 2 and 7. It was observed during all tests that slight movements of the model surface resulted in noticeable changes in the thermocouple temperature measurements. Since more Fiberfrax was used in the model-to-holder gap on Model Nos. 2 and 7, it is possible that model expansion was more restricted. This would cause model surface distortion resulting in the larger temperature spread that occurred.

Table XIII contains the thickness and weight change data for each model. The thickness data were obtained from pre-test and post-test measurements using a ball micrometer, and the weight data were obtained without the thermocouples attached using a Voland analytical balance. The greatest weight loss was experienced by the Haynes-188 material even though it was subjected to only 2000°F (1367 K).

## 5.2 Spectrographic measurements

During this test program, a spectrographic survey of the test stream and arc heater internal radiation was performed. The objective of the survey was to quantify the spectral radiation emanating from the arc heater and test stream and determine the resulting interference with the optical pyrometer operation.

Two types of measurements were made of the radiant background flux at two separate arc heater operating conditions. One of these arc heater conditions was the operating point at which the six model tests at 2200°F (1478 K) were conducted. The initial measurements were to determine the magnitude of the radiance from only the plasma stream. The second series of measurements determined the amount of radiant energy from the arc heater electrode region reflected at the test model surface into the pyrometer.

The results of these spectrographic measurements indicated that the radiance of the plume downstream of the nozzle exit was insignificant when compared with the radiance from the arc chamber region reflected from the model. The measured arc chamber radiance as a function of wavelength is shown in

## Table XIII Model physical characteristics

| Thickness (in.) (cm) at position (see Fig. 11) | Test model | | | | | | |
|---|---|---|---|---|---|---|---|
| | 1 (TD-NiCr) | 2 (TD-NiCrAlY) | 3 (DS-NiCr) | 4 (Haynes-188) | 5 (TD-NiCr) | 6 (DS-NiCr) | 7 (TD-NiCrAl) |
| M1 Pre | 0.0127 (0.0323) | 0.0140 (0.0356) | 0.0120 (0.0304) | 0.0168 (0.0426) | 0.0115 (0.0292) | 0.0115 (0.0292) | 0.0163(0.0414) |
| post | 0.0135 (0.0343) | 0.0150 (0.0381) | 0.0125 (0.0317) | 0.0180(0.0457) | 0.0110 (0.0279) | 0.0125 (0.0318) | 0.0170 (0.0432) |
| change | +0.0008 (0.0020) | +0.0010 (0.0025) | +0.0005 (0.0012) | +0.0012 (0.0030) | −0.0005 (0.0012) | +0.0010 (0.0025) | +0.0007 (0.0017) |
| M2 Pre | 0.0126 (0.0320) | 0.0140 (0.0356) | 0.0120 (0.0305) | 0.0168 (0.0426) | 0.0115 (0.0292) | 0.0115 (0.0292) | 0.0163 (0.0414) |
| post | 0.0132 (0.0335) | 0.0150 (0.0381) | 0.0130 (0.0330) | 0.0180 (0.0457) | 0.0110 (0.0279) | 0.0120 (0.0317) | 0.0170 (0.0430) |
| change | +0.0006 (0.0015) | +0.0010 (0.0025) | +0.0010 (0.0025) | +0.0012 (0.0030) | −0.0005 (0.0012) | +0.0005 (0.0025) | +0.0007 (0.0017) |
| M3 Pre | 0.0132 (0.0335) | 0.0140 (0.0356) | 0.0120 (0.0305) | 0.0168 (0.0426) | 0.0115 (0.0292) | 0.0115 (0.0292) | 0.0163 (0.0414) |
| post | 0.0135 (0.0343) | 0.0150 (0.0381) | 0.0125 (0.0330) | 0.0180 (0.0457) | 0.0110 (0.0279) | 0.0125 (0.0318) | 0.0173 (0.0439) |
| change | +0.0003 (0.0076) | +0.0010 (0.0025) | +0.0005 (0.0012) | +0.0012 (0.0030) | −0.0005 (0.0012) | +0.0010 (0.0025) | +0.0010 (0.0025) |
| M4 Pre | 0.0125 (0.0318) | 0.0140 (0.0356) | 0.0120 (0.0305) | 0.0168 (0.0426) | 0.0115 (0.0292) | 0.0115 (0.0292) | 0.0162 (0.0411) |
| post | 0.0135 (0.0343) | 0.0150 (0.0381) | 0.0125 (0.0330) | 0.0180 (0.0457) | 0.0112 (0.0279) | 0.0120 (0.0317) | 0.0170 (0.0430) |
| change | +0.0010 (0.0025) | +0.0010 (0.0025) | +0.0005 (0.0012) | +0.0012 (0.0030) | −0.0003 (0.0012) | +0.0005 (0.0025) | +0.0008 (0.0020) |
| M5 Pre | 0.0125 (0.0318) | 0.0142 (0.0360) | 0.0120 (0.0305) | 0.0168 (0.0426) | 0.0115 (0.0292) | 0.0115 (0.0292) | 0.0161 (0.0409) |
| post | 0.0130 (0.0332) | 0.0150 (0.0381) | 0.0130 (0.0330) | 0.0180 (0.0451) | 0.0120 (0.0317) | 0.0125 (0.0368) | 0.0170 (0.0430) |
| change | +0.0005 (0.0012) | +0.0008 (0.0020) | +0.0010 (0.0025) | +0.0012 (0.0030) | +0.0005 (0.0012) | +0.0010 (0.0025) | +0.0009 (0.0023) |
| M6 Pre | 0.0124 (0.0314) | 0.0145 (0.0368) | 0.0120 (0.0305) | 0.0168 (0.0426) | 0.0115 (0.0292) | 0.0115 (0.0292) | 0.0157 (0.0398) |
| post | 0.0134 (0.0340) | 0.0155 (0.0393) | 0.0130 (0.0330) | 0.0180 (0.0457) | 0.0120 (0.0317) | 0.0125 (0.0318) | 0.0161 (0.0409) |
| change | +0.0010 (0.0025) | +0.0010 (0.0025) | +0.0010 (0.0025) | +0.0012 (0.0030) | +0.0005 (0.0012) | +0.0010 (0.0025) | +0.0004 (0.0010) |
| M7 Pre | 0.0127 (0.0323) | 0.0145 (0.0368) | 0.0120 (0.0305) | 0.0168 (0.0426) | 0.0115 (0.0292) | 0.0115 (0.0292) | 0.0162 (0.0411) |
| post | 0.0135 (0.0343) | 0.0155 (0.0393) | 0.0125 (0.0330) | 0.0180 (0.0457) | 0.0110 (0.0279) | 0.0120 (0.0317) | 0.0170 (0.0430) |
| change | +0.0008 (0.0020) | +0.0010 (0.0025) | +0.0005 (0.0012) | +0.0012 (0.0030) | −0.0005 (0.0012) | +0.0005 (0.0012) | +0.0008 (0.0020) |
| M8 Pre | 0.0126 (0.0320) | 0.0145 (0.0368) | 0.0120 (0.0305) | 0.0168 (0.0420) | 0.0115 (0.0292) | 0.0115 (0.0292) | 0.0162 (0.0411) |
| post | 0.0140 (0.0356) | 0.0155 (0.0393) | 0.0125 (0.0330) | 0.0180 (0.0457) | 0.0112 (0.0284) | 0.0125 (0.0305) | 0.0173 (0.0439) |
| change | +0.0014 (0.0036) | +0.0010 (0.0025) | +0.0005 (0.0012) | +0.0012 (0.0030) | −0.0003 (0.0008) | +0.0010 (0.0025) | +0.0011 (0.0028) |
| M9 Pre | 0.0126 (0.0320) | 0.0145 (0.0368) | 0.0120 (0.0305) | 0.0168 (0.0420) | 0.0115 (0.0292) | 0.0120 (0.0305) | 0.0163 (0.0414) |
| post | 0.0138 (0.0350) | 0.0155 (0.0393) | 0.0130 (0.0330) | 0.0182 (0.0462) | 0.0110 (0.0279) | 0.0128 (0.0325) | 0.0175 (0.0444) |
| change | +0.0012 (0.0030) | +0.0010 (0.0025) | +0.0010 (0.0025) | +0.0014 (0.0036) | −0.0005 (0.0012) | +0.0008 (0.0020) | +0.0012 (0.0030) |
| **Model weights (g)** | | | | | | | |
| Pre | 15.787 | 17.261 | 14.918 | 23.316 | 14.231 | 14.844 | 19.352 |
| post | 15.790 | 17.312 | 14.906 | 23.225 | 14.224 | 14.852 | 19.371 |
| change | +0.003 | +0.051 | −0.012 | −0.091 | −0.007 | +0.008 | +0.019 |

Fig. 19. Also shown in Fig. 19 is the blackbody radiance for bodies at various temperatures.

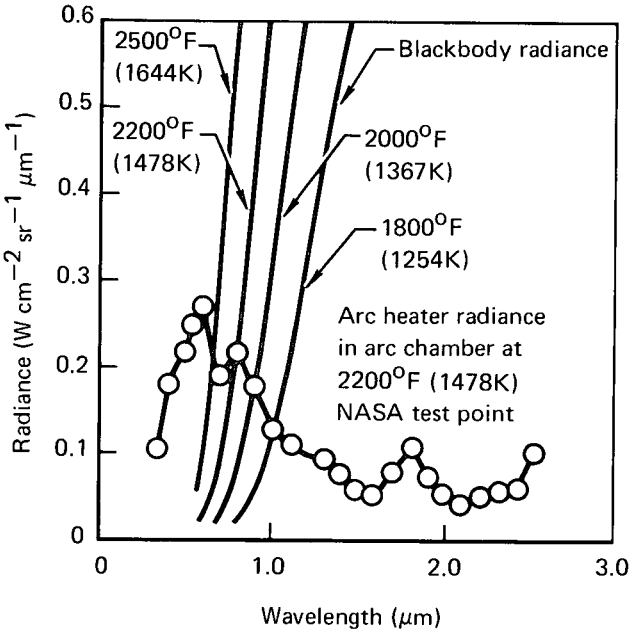


**Fig. 19 Background radiant flux from the PAT arc heater**

Superimposed on the plasma radiance curve in Fig. 19 are several blackbody radiance curves to indicate the relative magnitude of the plasma radiance. It is apparent that the arc heater reflected radiance contribution to the total energy incident on the pyrometer detector can be sizeable near 0.8 μm (the TD-9H pyrometer operating wavelength) at temperatures below 2500°F (1644 K). This results in masking any effect of model emittance change as shown in the following paragraphs.

The apparent radiance of the test model surface as measured by the pyrometer is the sum of that emitted by the model surface plus that emanating from the arc heater and reflected by the model surface. The radiosity as thus observed by the pyrometer can be expressed as:

$$W_a = \epsilon W_b + rG,$$

where

$W_a$ = apparent radiance as observed by pyrometer,

$\epsilon$ = emittance of model,

$W_b$ = blackbody radiance at model temperature,

$r$ = model reflectance, and

$G$ = arc heater radiance.

If

$$r = 1 - \alpha$$

where

$\alpha$ = absorptance,

and

$$\alpha = \epsilon,$$

then

$$r = 1 - \epsilon$$

and

$$W_a = \epsilon W_b + (1 - \epsilon) G.$$

Using the spectrographic measurement of arc heater radiance at a wavelength of 0.8 μm as obtained from Fig. 19, it can be shown that the effect of a large change in model emittance is insignificant on the apparent temperature observed by the pyrometer.

With

$G = 0.22$ W cm$^{-2}$ sr$^{-1}$ μm$^{-1}$, and

$W_b = 0.19$ W cm$^{-2}$ sr$^{-1}$ μm$^{-1}$ at 2200°F (1478 K),

then for

$\epsilon = 0.1$,

$$W_a = 0.1\,(0.19) + (1 - 0.1)\,0.22$$
$$= 0.019 + 0.198$$
$$= 0.217.$$

This corresponds to a blackbody temperature of 2227°F(1493 K).

With

$\epsilon = 0.9$, then

$$W_a = 0.9\,(0.19) + (1 - 0.9)\,0.22$$
$$= 0.171 + 0.022$$
$$= 0.193$$

which corresponds to a blackbody temperature of 2200°F (1478 K).

Thus, since the arc heater radiance at the operating condition for this test program is comparable to the blackbody radiance at 2200°F (1478 K), it is evident that the pyrometer is quite insensitive to model emittance change (change of 27°F (15 K) when emittance varied from 0.1 to 0.9). As a result, it is not possible to determine material emittance from the backface thermocouple outputs and pyrometer measurements since the accuracy of the pyrometer is ± 1% full scale or ± 25°F (14 K).

## 5.3 Photographs

Both pre-test and post-test color photographs were taken of each model. In addition, color photographs were made during selected test cycles to record certain events. To document the model appearance during the heating and cooling portions of a test cycle, a 16 mm color movie was made of several typical tests.

Figure 20 shows the backside of a typical sample with thermocouples attached while Fig. 21 gives a side view of the same sample. Figure 22 displays how the models were packed with Fiberfrax as backup insulation in the wedge holder. Figure 23 shows a typical instrumented sample installed in the wedge holder ready for installation in the test chamber. Figure 24 shows the typical appearance of one of the models during test. Figures 25 through 30 show the surface of model Nos. 2 through 7 after all cycle testing was complete. The post-test negative of model No. 1 was lost during processing.

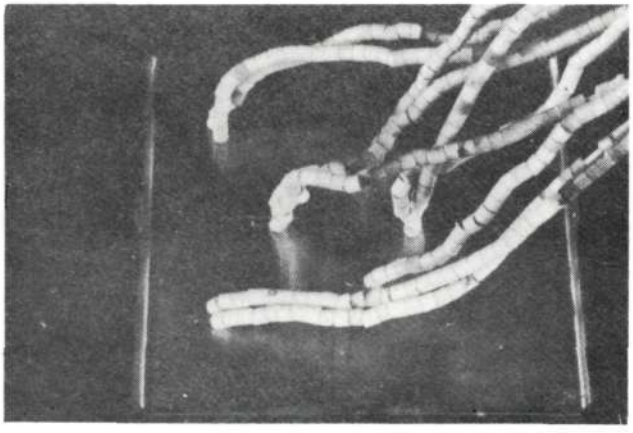

Fig. 20 Typical instrumented model backside

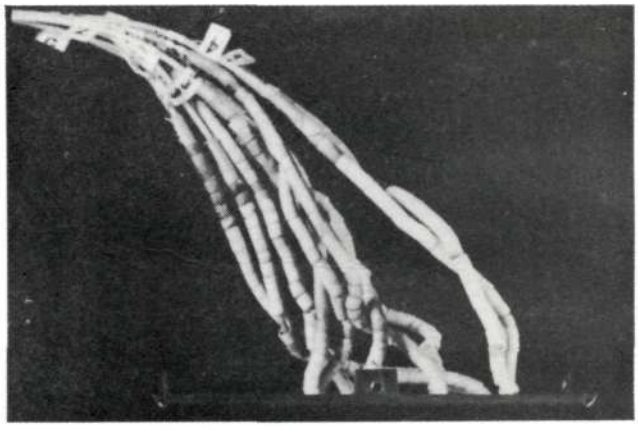

Fig. 21 Side view of typical instrumented model

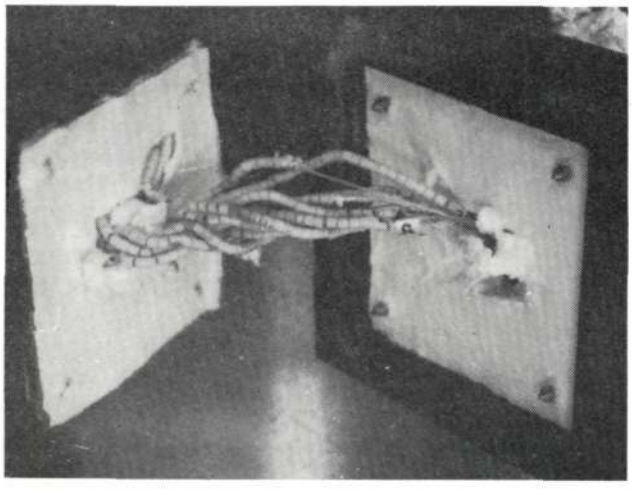

Fig. 22 Typical instrumented model with back-up insulation

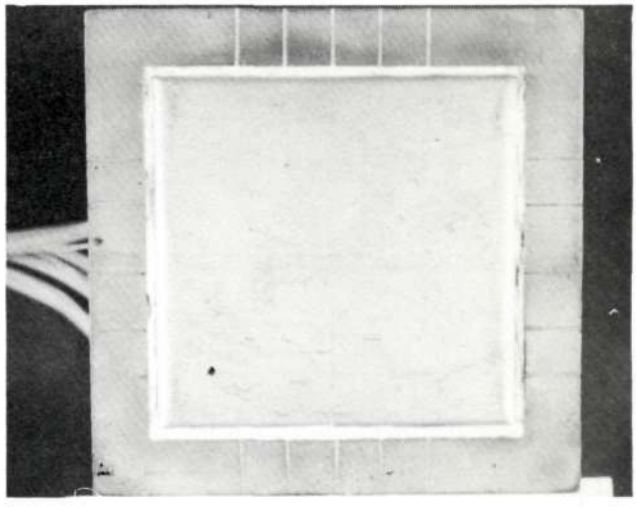

Fig. 23 Model installed in wedge holder

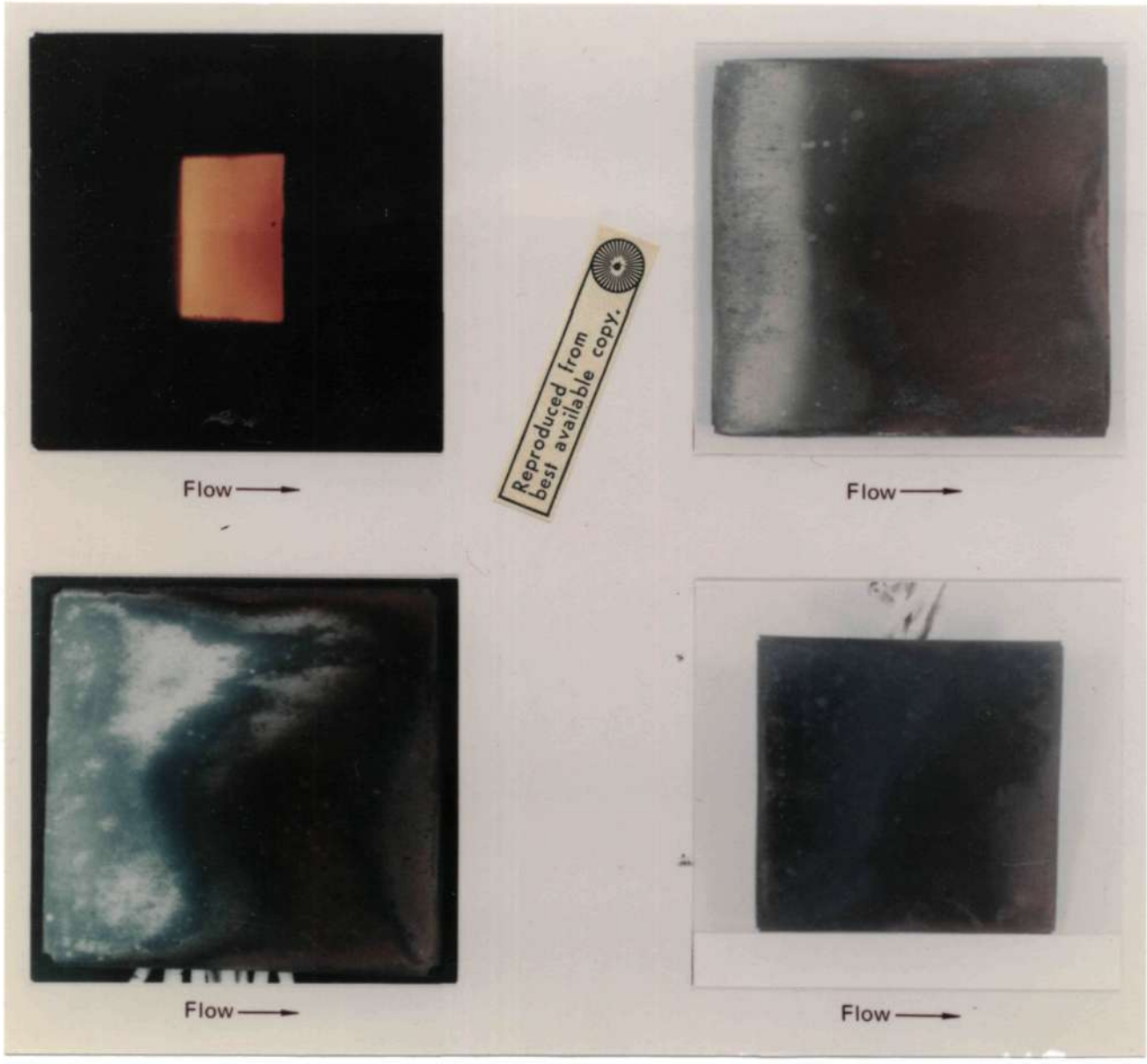




Fig. 24 (Upper left) Typical model appearance during test

Fig. 25 (Upper right) Model no. 2 (TC-NiCrALY) after 25 test cycles (10 min at 2200°F (1478 K) each cycle)

Fig. 26 (Lower left) Model no. 3 (DS-NiCr) after 25 test cycles (10 min at 2200°F (1478 K) each cycle)

Fig. 27 (Lower right) Model no. 4 (Haynes-188) after 25 test cycles (10 min at 2000°F (1367 K) each cycle)

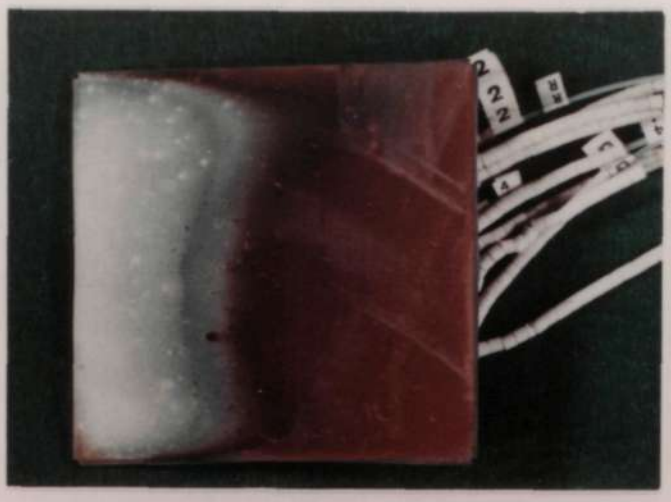

Flow →

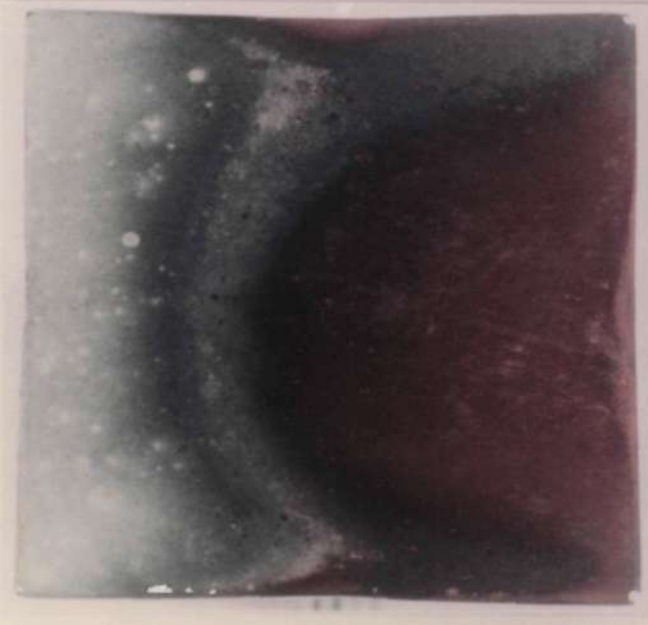

Flow →

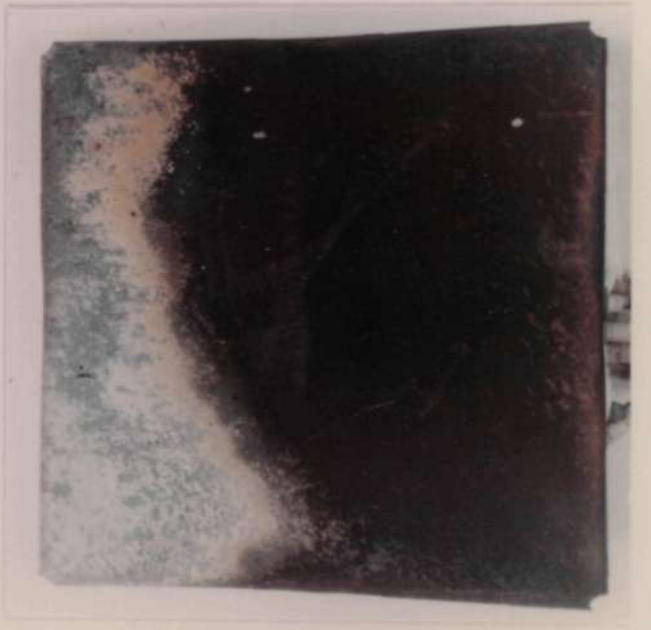

Flow →

Fig. 28 (Top center) Model no. 5 (TD-NiCr) after 50 test cycles (10 min at 2200°F (1478 K) each cycle

Fig. 29 (Lower left) Model no. 6 (DS-NiCr) after 50 test cycles (10 min at 2200°F (1478K) each cycle)

Fig. 30 (Lower right) Model no. 7 (TD-NiCrAl) after 25 test cycles (10 min at 2200°F (1478K) each cycle)

# 6 Concluding remarks

Four different nickel base alloys and one cobalt base alloy were evaluated for thermal protection system use on the space shuttle orbiter by subjecting 3.0 x 3.0 in. (7.6 x 7.6 cm) square models to an arc heater facility test stream. The metallic models were tested at 60 deg (1.05 rad) angle of attack with the leading edge temperature maintained at 2200°F (1478 K). The models were cycled at least 25 times each for 10 min each test cycle.

Conclusions drawn from this test program include:

1. It was necessary to fabricate the models to have a radius along each edge to maintain a relatively flat sample during test and cooldown periods.
2. No difficulty was experienced in tack welding the platinum-platinum 10% rhodium thermocouple wires to the backface of any of the test materials.
3. Material degradation as determined by thickness change (gross measurement including scale) was not evident in these tests.
4. The greatest weight loss was experienced by the Haynes-188 material (a cobalt base alloy) even though it was tested at a less severe condition (2000°F) (1367 K) and two other materials were tested twice as long (50 cycles vs 25 cycles). However, total model test times were too short to provide definitive patterns in material performance based on weight loss measurements only.
5. Optical pyrometer measurements were affected by the radiance from the arc chamber reflected off the model surface. As a result, it was not possible to determine model emittances by comparison of surface temperature pyrometer measurements and backface thermocouple measurements.

# 7 Reference

1. *"Hypervelocity Oxidation Tests of TD-NiCr Alloys," F. Centolanzi, NASA TMX-62015, 11 February 1971.*

# 8 Appendix A: Symbols

| | |
|---|---|
| A | calorimeter sensing area |
| $C_p$ | heat capacity of copper |
| d | diameter |
| G | arc heater radiance |
| m | calorimeter mass |
| M | Mach number |
| $P_{o2}$ | impact pressure |
| q | heat flux |
| r | model reflectance |
| $\Delta t$ | time differential |
| $\Delta T$ | temperature differential |
| W | radiance |
| $\alpha$ | absorptance |
| $\epsilon$ | emittance |

Subscripts

| | |
|---|---|
| a | apparent |
| b | blackbody |
| $\mathbb{Q}$ | centerline |
| cw | cold wall |
| ex | exit |
| m | model |

# 9 Appendix B: Distribution list

Mr. J. C. Freche (1)
MS 49-1
NASA Lewis Research Ctr.
21000 Brookpark Road
Cleveland, Ohio 44135

Mr. C. A. Barrett (1)
MS 49-1
NASA Lewis Research Ctr.
21000 Brookpark Road
Cleveland, Ohio 44135

Mr. M. Quatinetz (1)
MS 49-1
NASA Lewis Research Ctr.
21000 Brookpark Road
Cleveland, Ohio 44135

Mr. J. W. Weeton (1)
MS 49-1
NASA Lewis Research Ctr.
21000 Brookpark Road
Cleveland, Ohio 44135

Patent Counsel (1)
MS 500-311
NASA Lewis Research Ctr.
21000 Brookpark Road
Cleveland, Ohio 44135

Mr. J. Gangler/RWM (1)
NASA Headquarters
600 Independence Avenue
Washington, D.C. 20546

Library (1)
NASA
Ames Research Ctr.
Moffett Field, California 94035

Mr. R. W. Hall (1)
MS 105-1
NASA Lewis Research Ctr.
21000 Brookpark Road
Cleveland, Ohio 44135

Dr. H. B. Probst (1)
MS 49-1
NASA Lewis Research Ctr.
21000 Brookpark Road
Cleveland, Ohio 44135

Mr. N. T. Saunders (1)
MS 105-1
NASA Lewis Research Ctr.
21000 Brookpark Road
Cleveland, Ohio 44135

Library (2)
MS 60-3
NASA Lewis Research Ctr.
21000 Brookpark Road
Cleveland, Ohio 44135

Report Control Office (1)
MS 5-5
NASA Lewis Research Ctr.
21000 Brookpark Road
Cleveland, Ohio 44135

Mr. G. C. Deutsch/RW (1)
NASA Headquarters
600 Independence Avenue
Washington, D. C. 20546

Mr. J. Maltz / RWM (1)
NASA Headquarters
600 Independence Avenue
Washington, D. C. 20546

Library (1)
NASA
Goddard Space Flight Ctr
Greenbelt, Maryland 20771

Mr. B. Stein (1)
NASA
Langley Research Ctr.
Langley Field, Virginia 23365

Library (1)
NASA
Manned Space Flight Ctr.
Houston, Texas 77058

Mr. N. Geyer (1)
AFML/LLP
Headquarters
Wright Patterson AFB, Ohio 45433

Technology Utilization (1)
MS 3-19
NASA Lewis Research Ctr.
21000 Brookpark Road
Cleveland, Ohio 44135

Defence Documentation Ctr. (1)
Cameron Station
5010 Duke Street
Alexandria, Virginia 22314

MCIC (1)
Battelle Memorial Inst.
505 King Avenue
Columbus, Ohio 43201

Library (1)
NASA Flight Research Ctr.
P.O. Box 273
Edwards, California 93523

Library (1)
Jet Propulsion Laboratory
4800 Oak Grove Drive
Pasadena, California 91102

Dr. R. A. Anderson MS188 (1)
NASA
Langley Research Ctr.
Langley Field, Va. 23365

Library (1)
NASA
Langley Research Ctr.
Langley Field, Virginia 23365

Library (1)
NASA
Marshall Space Flight Ctr.
Huntsville, Alabama 35812

Mr. I. Machlin (1)
Bureau of Naval Weapons
Navy Department
Washington, D.C. 20525

Dr. B. Wilcox (1)
Battelle Memorial Inst.
505 King Avenue
Columbus, Ohio 43201

Library (1)
Cabot Corporation
Stellite Division
P.O. Box 746
Kokomo, Indiana 46901

Dr. F. Decker (1)
International Nickel Co.
Merica Research Lab
Sterling Forest
Suffern, N. Y. 10901

Mr. R. Perkins (1)
Matls. & Science Lab.
Lockheed Research Labs
3251 Hanover Street
Palo Alto, Cal. 94304

Library (1)
Pratt & Whitney Aircraft
United Aircraft Corp.
West Palm Beach, Florida 33402

Mr. L. P. Jahnke MPTL (1)
AETD
General Electric Company
Cincinnati, Ohio 45215

Mr. C. E. Cataldo S+Eastn-M (1)
NASA
Marshall Space Flight Ctr.
Huntsville, Ala. 35812

Contracts Section B (1)
MS 500-313
NASA Lewis Research Ctr.
21000 Brookpark Road
Cleveland, Ohio 44135

Mr. S. V. Arnold AMXMR-XW (1)
Army Materials and
Mechanics Research Ctr.
Watertown, Mass. 02172

Library (1)
Advanced Technology Lab
General Electric Company
Schenectady, N.Y. 12305

Dr. N. M. Parikh (1)
IIT Research Institute
10 West 35th Street
Chicago, Illinois 60616

Technical Information Ctr. (1)
Matls. & Science Lab.
Lockheed Research Labs
3251 Hanover Street
Palo Alto, Cal. 94304

Dr. J. S. Smith (1)
Chem & Met Division
Sylvania Electric Prod.
Towanda, Penna. 18848

Mr. E. F. Bradley (1)
Pratt & Whitney Aircraft
United Aircraft Corp.
400 Main Street
East Hartford, Conn. 06108

Mr. D. Goldberg (1)
Westinghouse Electric
Astronuclear Lab.
Pittsburgh, Penn. 15236

Mr. D. Maxwell (1)
International Nickel Co.
One New York Plaza
New York, N.Y. 10004

Library (1)
Denver Research Institute
University Park
Denver, Colorado 80210

Mr. D. Hanink Manager, (1)
Materials Laboratory
Allison Division
General Motors Corp.

Mr. J. V. Long (1)
Director of Research
Solar, Int. Harvester
2200 Pacific Highway
San Diego, Cal. 92112

Mr. R. A. Harlow (1)
Aeronutronic Division
Philco-Ford Corporation
Ford Road
Newport Beach, Cal. 92663

Library (1)
Materials Technology
TRW Equipment Group
23555 Euclid Avenue
Cleveland, Ohio 44117

Mr. H. K. Larson MS 234-1 (1)
NASA
Ames Research Ctr.
Moffitt Field, Ca. 94035

Dr. J. Colwell (1)
Aerospace Corporation
P.O. Box 95085
Los Angeles, Ca. 90045

Dr. D. H. Killpatrick (1)
McDonnell-Douglas Corp.
5301 Bolsa Avenue
Huntington Beach, Ca. 9264

Mr. E. F. Styer MS/8K-93 (1)
The Boeing Company
P.O. Box 3999
Seattle, Wash. 98124

Mr. L. A. Mead (1)
Grumman Aerospace Corp.
Plant 25
Bethpage, N. Y. 11714

Mr. C. S. Deneen (1)
Martin-Marietta Corp.
815 Connecticut Ave.
Washington, D.C. 20006

Mr. F. J. Demeritte / RV-1 (1)
NASA Headquarters
600 Independence Avenue
Washington, D.C. 20546

Mr. R. E. Vale Code ES (1)
NASA
Manned Space Flight Ctr.
Houston, Tex. 77058

Mr. W. L. Goesch (1)
AFDL/FDTS
Headquarters
Wright Patterson AFB, Ohio 45433

Dr. A. O. Tishler/Rp (1)
NASA Headquarters
600 Independence Avenue
Washington, D.C. 20546

Mr. R. E. Johnson ES8 (1)
NASA
Manned Space Flight Ctr.
Houston, Texas 77058

Mr. C. E. Tharratt (1)
Space Division
Chrysler Corporation
P.O. Box 29200
New Orleans, La. 70129

Mr. J. W. Davis / MS5101
McDonnell-Douglas Corp.
P.O. Box 516
St. Louis, Mo. 63166

Mr. N. Vojvodich (1)
NASA Ames Res. Center
Moffitt Field, Ca. 94035

Mr. R. A. Nau (1)
General Dynamics Corp.
P.O. Box 1128
San Diego, Ca. 92112

Mr. D. Cole / MC ESIZ (1)
NASA
Manned Spacecraft Center
Houston, Texas 77058

Mr. R. Johnson (1)
McDonnell-Douglas Corp.
A3-833 MS 9
Huntington Beach, Ca. 92647

Mr. George Glenn (1)
AFML/MATB
Headquarters
Wright Patterson AFB, Ohio 45433

Mr. B. Fitzgerald (1)
McDonnell-Douglas Corp.
P.O. Box 516
St. Louis, Mo. 63166

Mr. R. W. Fraser (1)
Sherritt-Gordon Mines
Fort Saskatchewan
Alberta
Canada

Mr. D. B. Arnold (1)
AETD
General Electric Co.
Cincinnati, Ohio 45215

Mr. L. Klinger (1)
Fansteel Inc.
Baltimore, Md. 21226

Mr. S. Kessler (1)
Materials and Process
Research Associates, Inc.
P.O. Box 527
Canoga Park, Ca. 91305

Mr. Frank Centolanzi (1)
NASA Ames Res. Center
Moffitt Field, Ca. 94035

Mr. Allen Hauser (1)
Pratt & Whitney Aircraft
United Aircraft Corp.
400 Main Street
East Hartford, Ct 06108

Dr. S. T. Wlodek (1)
Stellite Division
Cabot Corporation
1020 W. Park Ave.
Kokomo, In. 46901

Mr. W. E. Black (1)
Convair Division
General Dynamics Corp.
P.O. Box 1128
San Diego, Ca. 92112

Mr. C. P. Blankenship (1)
MS 105-1
NASA Lewis Research Ctr.
21000 Brookpark Road
Cleveland, Ohio 44135

The Marquardt Co. (1)
16555 Saticoy St.
Van Nuys, Ca. 91409

Mr. R. T. Torgerson (1)
Convair Division
General Dynamics Corp.
P.O. Box 1128
San Diego, Ca. 92112

Mr. A. E. Leach (1)
Bell Aerosystems Co.
Buffalo, N.Y. 14240

Mr. Jos. Trach (1)
MS 500-312
NASA Lewis Research Ctr.
21000 Brookpark Road
Cleveland, Ohio 44135

Mr. L. K. Crockett (1)
Space Division
North American Rockwell
12214 Lakewood Blvd.
Downey, Ca. 90241

Mr. D. L. Kummer (1)
McDonnell-Douglas Corp.
St. Louis, Mo. 63166

Mr. H. E. Hoercher (1)
AVCO Systems Div.
Wilmington, Mass. 01887

Mr. I. Grinberg (1)
Battelle Memorial Inst.
Columbus, Ohio 43201